NTNU

Norwegian University of
Science and Technology

In Vitro Setup for Coronary Circulation with Ventricular Motion

Alyssa Ninoska Garcia Mayuri

Master of Science in Cybernetics and Robotics
Submission date: June 2017
Supervisor: Hans Torp, ITK
Co-supervisor: Alfonso Rodriguez-Molares, Institutt for sirkulasjon og bildediagnostikk

Norwegian University of Science and Technology
Department of Engineering Cybernetics

Summary

Blood and tissue motion can be detected using Doppler ultrasound. However, in a complex system such as the human body, the blood is not the only matter in motion. Doppler signals reflected by blood are often disturbed by stronger signals generated by the surrounding tissue, a phenomenon referred to as clutter. Clutter signals, being generally $40 - 100$ dB stronger than the signals coming from blood, can usually be removed using conventional time filtering techniques. The problem arises when the surrounding tissue moves at velocities close to that of blood. In this case, conventional filters fail to remove the clutter components from the blood signal.

The aim of this thesis is to design and fabricate an in vitro phantom setup to evaluate ultrasound Doppler methods in coronary blood flow. For this, we propose an experimental setup consisting of a polyvinyl alcohol (PVA) heart ventricle and coronary artery phantom including coronary blood flow circulation. The ventricle motion can be controlled with a pulsatile flow into the ventricle's cavity or by moving the ultrasound probe with a 3D positioning system.

PVA phantoms were fabricated with 12 hour and 24 hour freezing-thawing (F-T) cycle. The mechanical properties such as the speed of sound and shear wave velocity were measured. The results from the characterization of the PVA phantoms show that the sound speed was held almost constant for all F-T cycles, with a variation of only 0.5%. The shear wave velocity for the 12h sample increased 0.82 m/s/cycle, and 0.46 m/s/cycle for the sample with a 24h F-T cycle. The results showed a high experimental uncertainty which does not allow us to state a relation between the samples with a 12h and 24h F-T cycle.

Different scenarios for tissue motion controlled by a pulsatile flow and a robot were conducted to check the performance of a standard clutter filter using different pulse repetition frequencies (PRF): Including no tissue motion, a 40 bpm tissue motion, and a 70 bpm tissue motion. The results show that the chosen filter works perfectly for a PRF of 10000 Hz. For a PRF of 5000 Hz, the filter performs flawlessly, except for tissue motion at 70 bpm where some tissue signal remained unfiltered although with little effect in the Power Doppler (PD) image. For a PRF of 2000 Hz, tissue signal remained unfiltered using a 40 bpm and 70 bpm tissue motion.
Our results show that, as expected, the quality of blood flow visualization decreases with decreasing PRF.

For the robot controlled tissue motion, the clutter filter fails to remove the clutter components from the blood signal. The PD image of the filtered signal spectrum is all smeared out and the blood flow is not displayed.

We have managed to reproduce ventricular motion in a coronary circulation in vitro setup. More work must be done to check the repeatability and reproducibility of that motion, the setup opens the possibility to test advanced clutter filtering techniques in a controllable environment.

Sammendrag

Doppler Ultralyd er en metode som kan brukes for å detektere bevegelser i blod og i vev. Men i et komplekst system som menneskekroppen, er ikke blodet det eneste som er i bevegelse. Doppler signaler reflektert av blod blir ofte forstyrret av sterkere signaler generert av det omkringliggende vevet, et fenomen som kalles for ≪clutter≫. Clutter signaler, som er vanligvis $40 - 100$ dB sterkere enn blodsignaler, kan vanligvis fjernes ved hjelp av konvensjonelle tidsfiltreringsteknikker. Problemet oppstår når det omkringliggende vevet beveger seg ved hastigheter nær blodets. I dette tilfellet, konvensjonelle filtrer feiler til å fjerne clutter komponentene fra blodsignalet.

Målet for dette prosjektet er å designe og produsere et in vitro fantom oppsett for å evaluere Doppler Utltralyd metoder i blodstrømningen i kransarteriene. For dette, vi foreslår et eksperimentelt oppsett bestående av et polyvinylalkohol (PVA) hjerteventrikkel og kransarterie fantom med blodsirkulasjonen i kransarteriene. Ventrikkelbevegelsen kan styres men en pulserende strømning i ventrikkelhulen , eller ved å flytte på ultralydproben med et 3D posisjoneringssystem.

PVA fantomene ble produsert med frysing-tining (F-T) sykluser av en varighet på 12 timer og 24 timer. De mekaniske egenskapene som lydhastigheten og skjærbølgehastigheten ble målt. Resultatene fra disse målingene viser at lydhastigheten ble holdt nesten konstant for alle F-T sykluser, med en variasjon på bare 0.5%. Skjærbølgehastigheten for fantomet med 12 timers F-T syklus økte med 0.82 m/s/syklus, mens økningen for fantomet med 24 timers syklus var på 0.46 m/s/syklus. På grunn av høy eksperimentell usikkerhet i resultatene, er vi ikke i stand til å kunne trekke en sammenheng mellom fantomene med 12 timers og 24 timers F-T syklus.

Det ble utført forskjellige scenarier for vevsbevegelse styrt av en pulserende strømning og en robot. Hensikten med dette var å vurdere prestasjonsevnen av et standard filter for clutter filtrering ved bruk av forskjellige pulsrepetisjonsfrekvenser (PRF): inkludert ingen vevsbevegelser, vevsbevegelser på 40 bpm og på 70 bpm. Resultatene viser at det valgte filteret fungerer utmerket for en PRF på 10000 Hz. For en PRF på 5000 Hz, filteret fungerer feilfritt, bortsett fra vevsbevegelsene på 70 bpm. For dette tilfellet forblir noe signal fra vevet ufiltrert, men med liten effekt i Power Doppler (PD) bildet av blostrømningen. For en PRF på 2000 Hz ble ikke signalet fra vevet filtrert bort for de tilfellene med vevsbevegelsene på 40 bpm og 70 bpm. Våre resultater viser, som forventet, at kvaliteten på bildet av blodstrømningen blir dårligere med avtagende PRF verdi.

For robotstyrt bevegelsen så klarte ikke filteret å fjerne clutter komponentene fra blodsignalet. PD bildet av det filtrerte signalspekteret er smurt ut og blodstrømmen er vises ikke.

Vi har klart å reprodusere ventrikulær bevegelse i en in vitro-kretsløpssirkulasjon. Mer

arbeid må gjennomføres for å kontrollere muligheten for å gjenta og reprodusere den bevegelsen, men dette oppsettet åpner muligheten for å teste avanserte clutter filtrering-steknikker i et kontrollerbart miljø.

Preface

This thesis is written as the last step for getting my masters degree in Cybernetics and Robotics at the Norwegian University of Science and Technology (NTNU). All the work has been done at the ultrasound laboratory at the Department of Circulation and Medical Imaging (ISB) at the Faculty of Medicine and Health Sciences at NTNU. The timeframe for this thesis has been the spring semester 2017, and it has been supervised by Professor Hans Torp and co-supervised by Post Doc and Senior Engineer Alfonso Rodriguez-Molares, both from ISB.

Acknowledgment

First, I would like to thank my supervisor Alfonso Rodriguez-Molares, for encouraging me to get out of my comfort zone and take upon this challenge. It has been a pleasure not only having him as my mentor but also as my friend. I really cannot imagine having a better supervisor. Without him and his ability to motivate and guide people, I would not have been able to enter the tunnel nor see the light at the end of it. I am really grateful for all the help, time and energy you have invested in me and my work. Sometimes you have helped me just by hearing mine complains about the weather or my allergies.
I would also like to thank those working at the ultrasound laboratory who came by from time to time to give me some advice and help me. Mostly Stefano who spend some hours helping me debug my code and sharing my frustration with the user interface for the robot.

Secondly, I would like to thank my family for daring me to dream big and always believing in me. Especially thank my mom, to whom I owe so much and has sacrificed everything so that I could have the opportunity of a better future. Also to my friends who became my family, thank you for all these years together, without all of you this adventure would just have been a journey.

Finally, I would like to thank my fiance Jon. I am grateful for the love and support all these years, and especially these last months. You are the love of my life, and I am glad that you still want to marry me after this semester.

Trondheim, 21 June 2017
Alyssa N. Garcia M.

Contents

List of Tables

List of Figures

Abbreviations

ARFI	:	Acoustic Radiation Force Impulse
BNC	:	Bayonet Neill–Concelman
CCA	:	Common Carotid Artery
CHD	:	Coronary Heart Disease
CPWI	:	Compound Plane Wave Imaging
CVD	:	Cardiovascular Disease
CW	:	Continuous-Wave
Cx	:	Circumflex
TDI	:	Doppler Tissue Imaging
F-T	:	Freeze - Thaw
GUI	:	Graphical User Interface
LAD	:	Left Anterior Descending
MI	:	Myocardical Infarction
PD	:	Power Doppler
PRF	:	Pulse Repetition Frequency
PVA	:	Polyvinyl Alcohol
PW	:	Pulsed-Wave
PWI	:	Plane-Wave Imaging
RCA	:	Right Coronary Artery
ROI	:	Region of Interest
SNR	:	Signal-to-Noise Rate
SSI	:	Supersonic Shear Imaging
SWE	:	Shear Wave Elastography
SWV	:	Shear Waves Velocity
TTE	:	Transthoracic Echocardiography
WWI	:	World War I
WWII	:	World War II

Chapter 1

Introduction

1.1 Problem Statement

Ultrasound blood flow imaging is hampered by noise produced by other structures such as muscles, fat tissue, and blood vessel walls. We refer to this noise as clutter. The clutter signal can be $40 - 100$ dB stronger than the signal coming from blood [1]. Clutter noise, contrary to the signal scattered by blood, is quasi-static (slowly moving). This makes it possible, in many situations, to use time filtering techniques to compensate for such low signal-to-noise ratio. But in some other situations, the structures that generate clutter, such as the heart ventricle or the artery walls, move at a velocity similar to that of the blood flow. In those situations, conventional clutter filters fail.
Advanced clutter filtering techniques have been proposed to address this problem, but it is difficult to compare the performance of different approaches in in vivo scenarios because the ground truth is often ignored.

1.2 Objectives

The main objective of this project is to design, and fabricate an in vitro phantom setup to evaluate ultrasound Doppler methods in coronary blood flow. The project can be divided into the following tasks:

- Design of an experimental setup for coronary blood flow with known ground-truth, using a robot 3D positioning system.
- Design and fabrication and characterization of polyvinyl alcohol (PVA) phantoms of healthy coronary arteries.
- Design and fabrication and characterization of a PVA phantom of a heart ventricle including coronary circulation.

- Test the phantoms on the experimental rig and check the performance of conventional clutter filtering techniques.

1.3 Myocardial Infarction

Myocardial Infarction (MI) is the medical term for heart attack, a life-threatening medical condition that should be treated immediately [2]. MI occurs when the blood supply to the heart is blocked, which can cause tissue damage. This damage can be irreversible if the blockage lasts too long, as the lack of oxygen causes the heart tissue to starve and die [2].

Coronary heart disease (CHD), also called coronary artery disease (CAD), is a serious condition that affects 32.4 million people worldwide every year [3, 4]. The aorta, which is the main blood supplier to the body, branches off into two coronary arteries situated on each side of the heart. The right coronary artery supplies blood mainly to the right side of the heart through smaller arteries, while oxygen-rich blood to the left side of the heart is delivered by the small arteries from the left coronary artery [5]. CHD is caused by the building of plaque on the inside walls of these major blood vessels causing a narrowing of the coronary arteries, and thus a reduction of blood flow to the heart muscle [5]. Plaque is made up from various substances such as fat, calcium, cholesterol, etc; and it builds up over many years. Over time, plaque can rupture, and the platelets (tiny blood cells that aid clotting) stick to the side of the injury. Eventually, platelets can clump together developing a blood clot at the site of the rupture, which can block the blood flow [5, 6]. Figure 1.1, taken from [7] illustrates some elements of a heart attack: the narrowing of the coronary arteries, a blood clot blocking two arteries, and the formation of necrotic tissue.

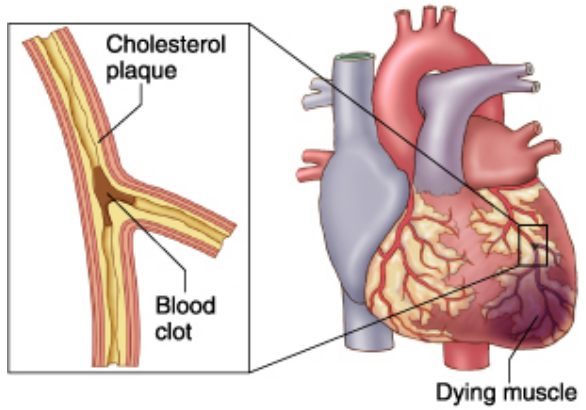

Figure 1.1: The building up of plaque inside the walls of the arteries can cause a narrowing of the coronary arteries. This narrowing can lead in many cases to a myocardial infarction. Adapted from [7].

Although it is still unclear why plaque builds up, there are certain factors that can

increase the risk of having CHD. Some risk factors can be controlled, such as smoking, the lack of physical activity, an unhealthy diet and thus obesity. While others cannot, such as genetics and age [5].

1.4 Ultrasound

Some animals such as dolphins and bats use the reflection of sound to locate objects. Diagnostic ultrasound imaging is built upon this principle. The connection between echolocation and medical imaging, however, was not made until the science of underwater exploration was mature [8].

”To sound” means to measure the depth of the sea water, according to [8]. The ancient Greeks probed the depths of the sea with a ”sounding machine”, which consisted of a long rope knotted at regular intervals with a lead weight at the end. Even though the sound was not used in the ancient sounding machine, the term ”to sound” set the stage for the later use of actual sound for the same purpose [8]. The sounding machine method was in continuous use for thousands of years until it was replaced by ultrasound echo-ranging in the twentieth-century [8].

The beginnings of sound navigation and ranging (sonar), and ultrasound for medical imaging can be traced back to the start of the twentieth-century. Even though there was no practical way of implementing underwater echo-ranging detection, shortly after the Titanic tragedy, L. F. Richardson filed patents to detect icebergs using echo-ranging in 1913 [8]. The discovery of piezoelectricity by the Curie brothers in 1880, and the invention of the triode amplifier tube by Lee De Forest in 1907 made way for further advances in pulse-echo range measurement. By the end of World War I (WWI), C. Chilowsky and P. Langevin took advantage of these enabling technologies to build high-power echo-ranging systems to detect submarines. During transmissions, ultrasound-induced bioeffects such as floating death fish, were discovered. This event started an intense period of experimentation and hopefulness. After WWI, researchers began to determine the conditions under which ultrasound was safe [8].

During World War II (WWII), some medical practitioners saw the possibilities of using pulse-echo techniques to probe the human body for medical purposes [8]. In 1946, Floyd Firestone invented the supersonic reflectoscope which applied the pulse-echo ranging principle to the location of defects in metals in the form of a reasonably compact instrument [8, 9].

A new world of possibilities for medical diagnosis was born, when commercialized versions of the reflectoscope were applied to the human body in many countries. In Sweden in 1953, Dr. I. Edler and Professor C. H. Hertz detected heart motions with a flaw detector and began the application of ultrasound to the characterization and imaging of the heart [8].

1.5 Cardiac Ultrasound

Cardiac ultrasound, also called echocardiography, refers to the use of ultrasound waves to image the heart and its blood vessels. This is done in order to get information such as the heart size, shape, and motion [8]. Blood and tissue motion can be detected using Doppler ultrasound, which is enabled by the Doppler effect. The Doppler effect is the change in the observed frequency of the sound wave compared to the emitted frequency, which occurs due to the relative motion between the observer and the source [10]. If there is no motion, the observer detects the frequency of the received pulse as equal to the transmitted frequency. If the source moves towards or away from the observer, the frequency detected by the observer is higher or lower than the transmitted frequency, respectively. This change in the observed frequency is known as Doppler shift. The magnitude of the Doppler shift frequency is proportional to the relative velocity between the source and the observer [10].

The Doppler effect enables to estimate blood velocity by measuring the change in the frequency of the ultrasound scattered by the moving blood. In this case, the transducer is held stationary while the blood moves in respect to it. Doppler systems often provide both spectral Doppler displays and Color Doppler images. Both techniques use the Doppler effect to obtain information about the blood flow [10]. In 2D Color Doppler, the 2D image in which blood velocity is color-coded, and superimposed on the B-mode image allowing rapid visualization of the flow patterns in vessels. The color represents the Doppler shift for each pixel, averaged over the area of the pixel. With this technique, high-velocity jets in arteries and in cardiac chambers can be seen. With Color Doppler display, blood flow within a large area of the tissue can be observed. Figure 1.2 shows a Color Doppler image of the blood flow in the common carotid artery (CCA).

In spectral Doppler, the Doppler frequency shift is displayed versus time in the form of a frequency shift-time plot. The spectral Doppler display allows for a closer inspection of the changes in velocity over time within a single small area. A spectral Doppler system uses the changes in blood velocities that occur across a narrowing, not only to identify the presence of a stenosis, but also to quantify the degree of the narrowing [10]. Figure 1.3 shows the spectral Doppler display of an arterial blood flow.

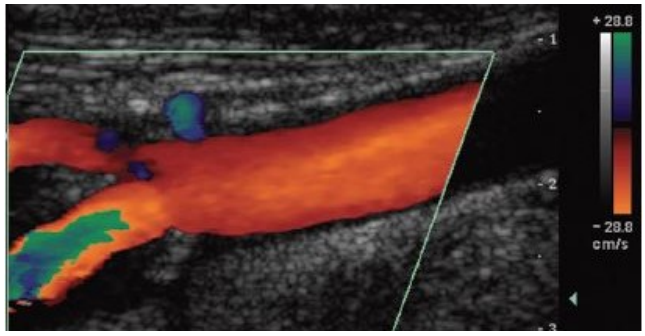

Figure 1.2: Color Doppler image of common carotid flow with a blue-red scale, in which the colors represent the direction of the blood flow. Adapted from [10].

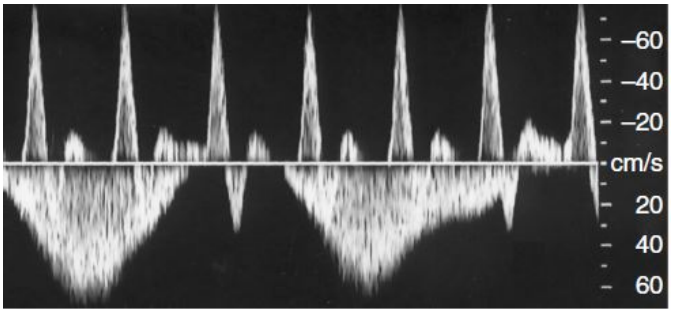

Figure 1.3: Spectral Doppler display showing arterial flow towards the transducer displayed above the baseline, and venous flow away from the transducer displayed below the baseline. Adapted from [10].

Doppler systems can be classified as pulsed-wave (PW) or continuous-wave (CW) systems, depending on whether the ultrasound is transmitted as short pulses or continuously, respectively. A CW Doppler system consists of at least two transducer elements: one to continuously transmit, and one to continuously receive. For a PW Doppler system, the same transducer element can be used to transmit and receive the pulse. Doppler signals in PW are determined by the depth and length of the pulse, while in CW, the Doppler signal is determined by the overlap of the transmitted and received ultrasound beams. In either case, the received ultrasound signal is processed by the Doppler signal processor in order to extract the Doppler frequency shifts. These are then displayed in either Color Doppler or spectral Doppler [10]. Figure 1.4 [11] illustrates the PW and CW Doppler principles.

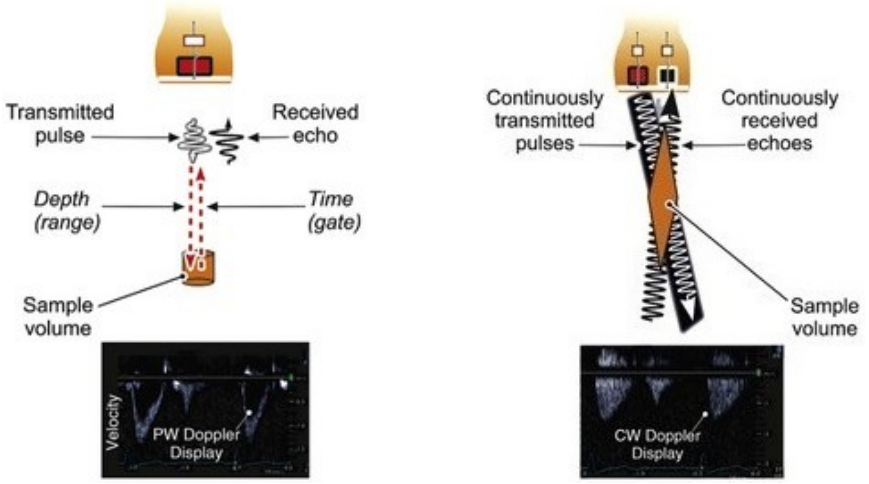

Figure 1.4: The PW Doppler technique (left) uses a single element to transmit a pulse through a sample of a specific depth and receives the echoes emerging thereof. The CW Doppler technique (right) uses separate elements that continuously transmit pulses, and receive echoes from a large sample. Adapted from [11].

Tissue Doppler Imaging (TDI) is a modification of the Color Doppler which obtains information on tissue motion using the Doppler effect. Velocities in tissue are often lower than in blood, this is accounted for by lowering the velocity scale. Having obtained the velocity information at each pixel in the image, it is possible to estimate how much and how fast the tissue is stretched or compressed [10]. This technique is the principle that makes sonoelastography possible: the estimation of tissue elasticity with ultrasound.

1.6 Ultrasound Vascular Imaging

Vascular Ultrasound imaging is a noninvasive ultrasound method used to examine the circulation in blood vessels [12]. Color flow images can reveal the presence of a narrowing of the blood vessels, or other flow patterns associated with cardiovascular disease (CVD). The location and quantification of CVD may be possible by measuring the changes in velocity of the blood, or by the shape of the Doppler spectrum [10].

The artery walls consist of a three-layer structure: the intima which is the inner layer, the media and the adventitia which are the middle and outer layer, respectively [10, chap.8]. The intima is a thin layer of endothelium overlying an elastic membrane, the media consists of smooth muscle and elastic tissue, while the adventitia is predominantly composed of connective tissue with collagen and elastic tissue. Cardiovascular disease can cause a change in the wall structure of the arteries, such as the thickening of the intima wall that can lead to the narrowing of the blood vessels (stenosis) as it can be seen in Figure 1.5 [10].

Figure 1.5 illustrates stenotic blood flow:

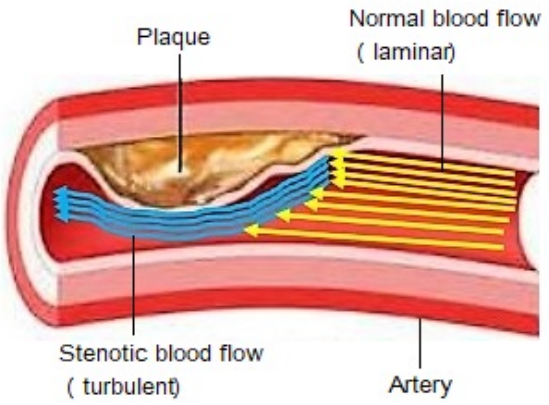

Figure 1.5: Stenosis can cause the normal blood flow to break down into a turbulent blood flow due the narrowing of the vessel walls. Adapted from [13].

The blood flow in normal arteries at rest is laminar, while the presence of turbulent flow may be a sign of disease. In laminar flow, the blood moves in layers, with one layer

sliding over the other at different velocities. In the case of an artery disease such as stenosis, the velocity increases, causing the laminar flow to break down into a turbulent flow. In a turbulent flow, the blood moves randomly in all directions at variable speeds, but with an overall forward flow velocity [10].

Turbulent flow, and thus the presence of disease, can be detected with spectral Doppler. This can be seen by the spectral broadening due to the range of velocities present within the turbulent flow as shown in Figure 1.6. High blood velocities also indicate the narrowing of blood vessels. As seen in Figure 1.6a, a maximum velocity of -0.4 m/s corresponds to the velocity in a normal section, while in Figure 1.6b the maximum velocity in a stenotic region is -4.2 m/s.

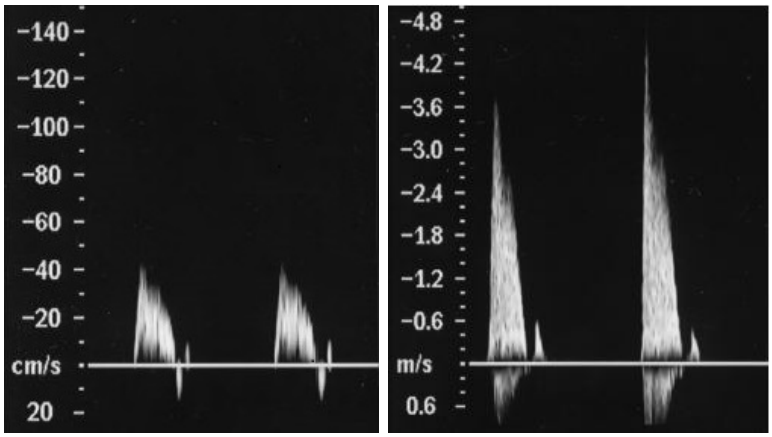

(a) Normal section with a maximum velocity of -0.4 m/s.

(b) Stetonic section with a maximum velocity of -4.2 m/s.

Figure 1.6: Doppler signal obtained (a) proximal to and (b) with a significant stenosis demonstrating a velocity increase from -0.4 m/s to -4.2 m/s. Adapted from [10].

The velocity profile across an artery varies over time due to the variation of blood velocities. This velocity variation is caused by the pulsation of the blood flow. The velocity and direction of the flow are dependent on the pressure drop along the length of the vessel. The pressure pulse produced by the heart travels down the arterial tree, and is modified by the pressure wave that has been reflected back from the distal vessels. A reversal flow during a cardiac cycle arises due to high distal resistance to the flow and affects the velocity profile seen in the vessel. Color flow imaging can be used to observe these changes in flow direction during the cardiac cycle.

1.7 Coronary Artery Imaging using Ultrasound

The diagnosis of coronary artery anomalies is usually performed by an imaging technique called angiography [14]. Coronary angiography is a method used to visualize the coronary

arteries using x-ray imaging. However, this is an invasive procedure that requires cardiac catheterization where contrast dye (usually containing iodine) and x-ray imaging are used to detect blockages in the coronary arteries [15]. The emerge of new cardiac imaging techniques, and the miniaturization of ultrasonic probes have made way for common methods such as transthoracic echocardiography (TTE). TTE is a sensitive and highly specific non-invasive method using Doppler ultrasound for imaging of coronary artery occlusions [16]. Although, the entire arteries cannot be imaged using TTE, useful anatomic and physiologic information can be obtained by visualizing multiple long segments of the coronary arteries and measuring the blood flow velocities through the arteries [17].

The development of high-frequency transthoracic transducers and the second harmonic tissue imaging technology have allowed the application of TTE to be widely used for diagnosis of coronary narrowing [16]. TTE can be successfully performed using a high-frequency ultrasound diagnostic system and a phased array ultrasound probe. The patients should be positioned in the left lateral decubitus position for the ultrasound beam direction to be parallel to the blood vessel when placing the probe on the patient's chest [16]. This is done in order to avoid the beam being reflected and to increase the signal penetration and thus the quality of the image. For increased visualization, the coronary arteries are each divided into three segments of approximately same length. TTE allows for the direct, transthoracic visualization of multiple segments of the coronaries such as the left anterior descending (LAD), circumflex (Cx), and the right coronary artery (RCA) as shown in Figure 1.7.

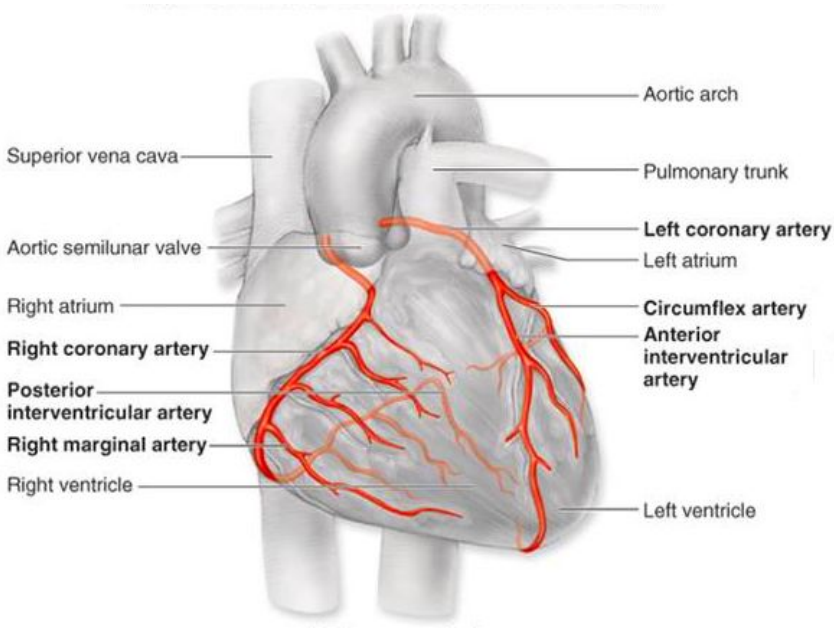

Figure 1.7: Coronary arteries anatomy and positioning on the heart muscle. Adapted from [18].

Color Doppler coronary artery mapping is used to search for the exact location of the coronary arteries and identify the direction of coronary blood flow. PW Doppler technique placed on the color signal can be used to register blood flow velocity patterns after the arteries are located. Spectral Doppler can also be used to assess the velocity of the blood flow through the coronary arteries [16].

1.8 Structure of the Report

The following chapter, chapter 2, covers the basic theory necessary to understand the methods and results from all the experimental work done. The materials and methods used to carry out the investigation are described in Chapter 3, followed by the results in Chapter 4. The validity of the results are further discussed in Chapter 5. This chapter presents also the conclusions of this thesis and future work.

Chapter 2

Theory

For this project, we propose an experimental setup consisting of a PVA heart ventricle and coronary artery phantoms to simulate the coronary blood flow circulation. The ventricle motion can be controlled with a pulsatile flow into the ventricle's cavity or by moving the ultrasound probe with a 3D positioning system.

This chapter covers the principles of sound wave propagation in tissue, the PVA phantom fabrication and characterization methods, and ultrasound imaging techniques such as plane wave imaging and clutter filtering. Finally, the 3D positioning system for the ventricle motion is described.

2.1 Acoustic Wave Propagation

Acoustic energy is transmitted as a sound wave propagates through a medium. A sound wave is a disturbance with a regularly repeating pattern, which travels from one point to another. When a sound wave is reflected it carries information about the domain back to the imaging system [10, 8]. Because of the high water content in tissue, wave propagation in tissue is simplified to be approximately as in liquids. In reality, tissues are elastic media with complex structures and other types of waves can propagate. The main difference between waves in solids and fluids is that only longitudinal waves exist in fluids, also called compressional waves. Other types of waves are possible in solids, such as shear waves, also called transverse waves [8].

Figure 2.1 shows the propagation of a sound wave through a fluid - solid interface. A longitudinal wave with an angle of incidence θ_{1L} on the surface of a solid creates a longitudinal wave and a shear wave with their corresponding angle of incidence θ_{2L} and θ_{2SV}, respectively; as seen in Figure 2.1. A reflected shear wave is not generated, as it is not supported in liquids; however, a longitudinal wave θ_R will be reflected at the interface between two solids [8].

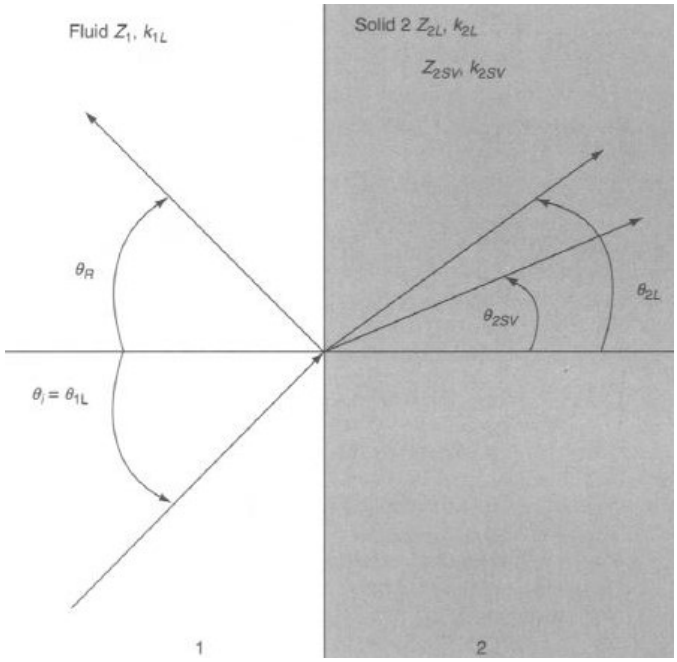

Figure 2.1: Wave-vectors in the x-z plane for a fluid-solid interface problem [8].

2.1.1 Longitudinal Waves

Longitudinal waves are generated as a result of pressure change within a material as it is stretched or compressed. By subjecting a cube of tissue of volume V to a pressure P on all sides results in a change in pressure to P+ δP, causing a reduction in volume by an amount δV [10]. Figure 2.2 shows the effect of tissue compression:

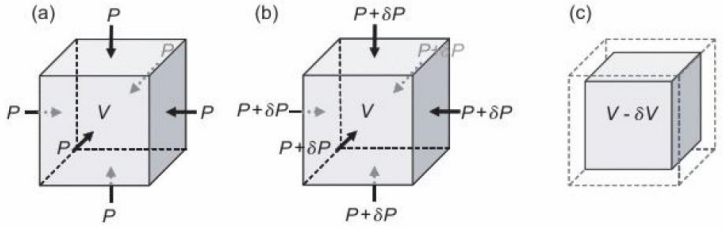

Figure 2.2: Compression occurs due the increase in pressure within a material, which results in the reduction of its volume. Adapted from [10].

In longitudinal waves the tissue moves to and fro in the same direction as the wave motion as illustrated in Figure 2.3:

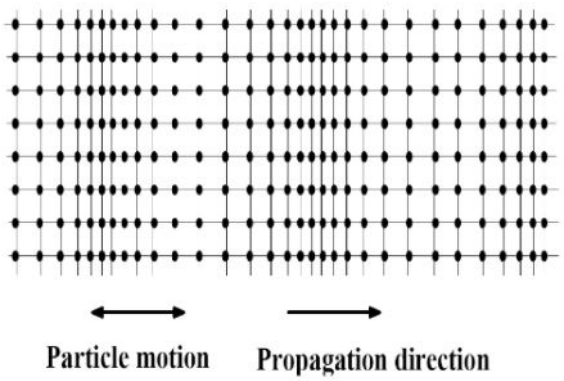

Figure 2.3: The particles motion in longitudinal waves is along the direction of propagation. Adapted from [19].

The velocity of the pressure wave as it propagates through a medium can be estimated by:

$$v_l = \sqrt{\frac{B}{\rho}} \tag{2.1}$$

where B is the bulk modulus which describes the change in volume of a material due to compression, and ρ is the average density of the material [10].

2.1.2 Shear Waves

Shear waves cannot occur in liquids; they are generated when a shear force is applied to the surface of a solid material. When a cube is subjected to a shear force parallel to one surface, the surface will be dragged in the same direction of the force. As the shear force is transmitted through the rest of the cube, the cube is distorted or sheared in the direction of the force as it can be seen in Figure 2.4 [10].

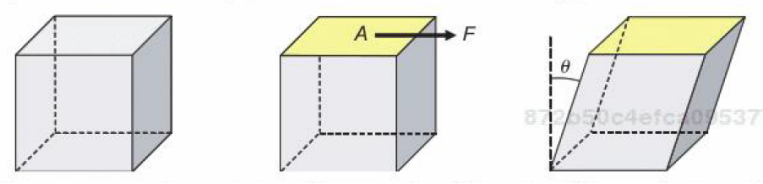

Figure 2.4: As a shear force F is applied to a cube material, the surface A will be dragged in the direction of the force by an angle θ. Adapted from [10].

Shear waves are generated and travel through the material as a result of this applied shear force. Particle motion in shear waves is illustrated in Figure 2.5. Shear waves are also called transverse waves, as the shear wave particles move transverse to the wave motion.

At any one point, the material oscillates to and fro perpendicular to the direction of motion of the wave [10].

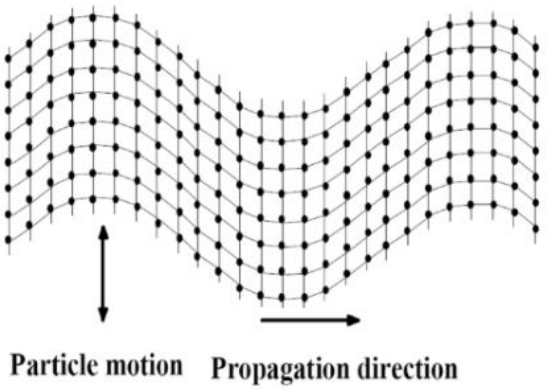

Figure 2.5: Shear waves- particles move perpendicular the direction of propagation. Adapted from [19].

Shear wave velocity depends on the local material density and the local elastic modulus:

$$v_s = \sqrt{\frac{G}{\rho}} \tag{2.2}$$

where G is the shear modulus which describes the ability of the material to withstand a shear force, and ρ is the density of the material. There is no change in density with time as the shear wave propagates. Shear waves are generated in the frequency range of $10 - 500$ Hz, and the speed of propagation of shear waves is typically between $1 - 10$ m/s [10].

The passage of shear waves relies on the ability of adjacent elements of the tissue to remain connected while the shear force is applied. The application of a shear force in a fluid results in gross motion of the fluid, causing the disconnection of adjacent elements.

2.2 Plane wave Imaging

As mentioned in Section 2.1.2, the speed at which shear waves propagates is governed by the shear modulus. The shear modulus is used to measure the stiffness in materials. Plane wave imaging, a method that enables very high-frame-rate imaging, it is used to track shear waves as they propagate through tissue [10].

In the single plane wave technique, all array elements are activated in transmission to produce a plane wave in order to insonate the whole field of view in one pulse, hence allowing very high-frame-rate imaging of several thousand frames per second. An image is produced by the focusing of the received echoes using conventional beamforming techniques [10].

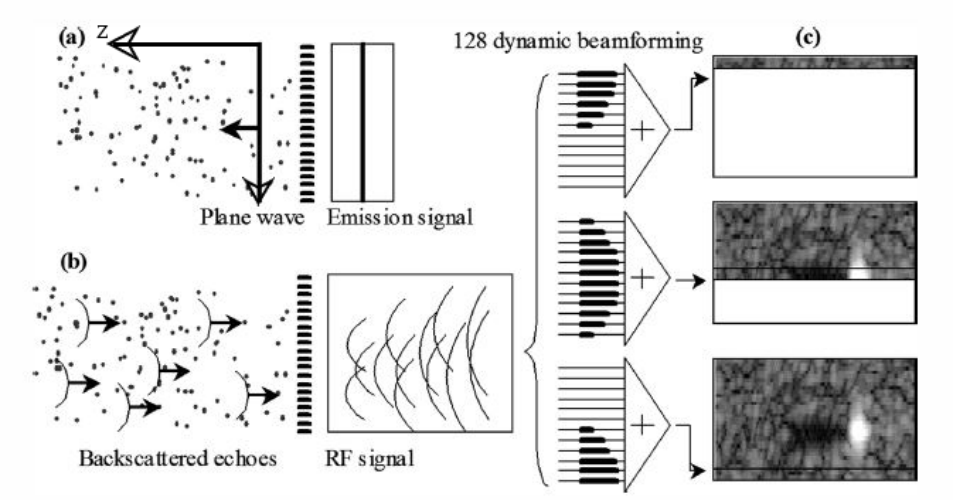

Figure 2.6: Schematic representation of the single transmit plane wave method. Adapted from [20].

To obtain a plane wave image, a linear array with typically 128 array elements is placed directly in contact with the imaging mediums surface. As it can be seen in Figure 2.6 (a), the x direction is parallel to the array, while the z direction is perpendicular to the array and indicates the depth of the medium. The medium is insonified by transmitting a large beam made of a unique pulsed plane wave (Figure 2.6 (a)). The plane wave is backscattered and the echo signals RF(x_1, t) are recorded by the transducer array, Figure 2.6 (b). Ultrafast imaging is achieved by simultaneously producing the entire frame from a single acoustic pulse with parallel processing in reception mode. Each point (x, z) of the image is obtained by adding coherently the echoes coming from the same scatter. In other words, delaying the RF(x_1, t) signals by $\tau(x_1, x, z)$ and adding them in the array direction x_1 [20]:

$$s(x, z) = \int_{x-a}^{x+a} RF(x_1, \tau(x_1, x, z))dx_1 \tag{2.3a}$$

where a is the aperture only from the active transducer elements that contribute to the signal [20]. Equation 2.3b is the traveling time to the point (x, z) and back to the transducer placed in x_1, given the speed of sound in the medium c:

$$\tau(x_1, x, z) = \frac{(z + \sqrt{z^2 + (x - x_1)^2}}{v_l} \tag{2.3b}$$

The single plane wave approach provides the fastest imaging method, but with a reduction in the image quality due to the lack of focusing in transmission. Image compounding is used to improve the image quality by obtaining plane waves of different angles in a coherent way to resynthesize the transmit focusing [20].

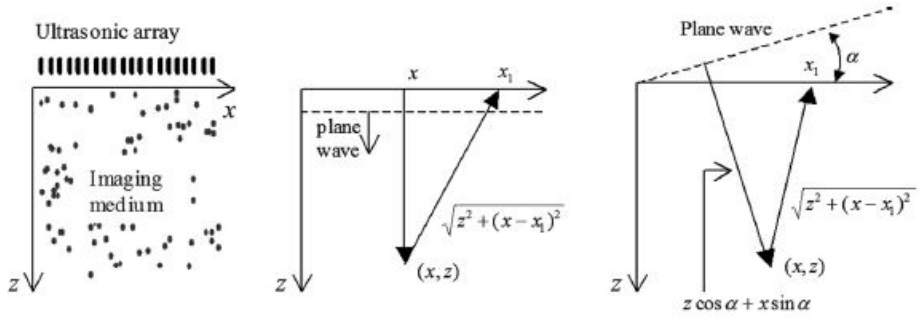

Figure 2.7: Plane wave imaging with single plane wave and coherent compound method. Adapted from [20].

By transmitting a plane wave with an inclination α as Figure 2.7 shows (right), the travel time to a point (x,z) in the medium is

$$\tau_{ec}(\alpha, x, z) = \frac{(z\cos\alpha + x\sin\alpha)}{v_l} \tag{2.4}$$

and the travel time back to the transducer placed in x_1 is

$$\tau_{rec} = \frac{\sqrt{z^2 + (x - x_1)^2}}{v_l} \tag{2.5}$$

The total 2-way travel time τ, for a plane wave insonification can be calculated:

$$\tau(\alpha, x_1, x, z) = \tau_{ec} + \tau rec \tag{2.6}$$

The image is obtained the same way as described above and depicted by Figure 2.6, but with the delays from Equation (2.6) [20].
By compounding coherently the images obtained with several planes waves of different angles, the image quality is increased. For this, a set of n plane waves with inclination angles $\tau_i, i = 1, ..., n$ is chosen and an image is built for each plane wave following the procedure described above for a single plane wave. All images are then added coherently to obtain a final compounded image [20].

2.3 Clutter Filtering

Clutter refers to the signals coming from slowly moving, or stationary tissue. Multiple reflections in tissue layers near the ultrasound probe cause multiple copies of the tissue signal, or reverberations, which can interfere with the blood signal [21]. Clutter filters are used to attenuate these unwanted signals. Without sufficient clutter rejection, low blood flow velocity cannot be measured, and the estimation of higher velocities will have a large bias [1, 22].

Doppler signals from blood have low amplitude and higher Doppler frequency shift than signals coming from tissue, which makes it possible to distinguish them in the frequency domain. A filter is usually characterized by its amplitude response, which is the

attenuation as a function of input frequency. The stopband and passband of a filter consist of the frequencies that are to be attenuated (stopped), and those which are allowed to pass through the filter, respectively. The required stopband magnitude of each filter may vary with its application. Between the stopband and the passband is the transition band [21].

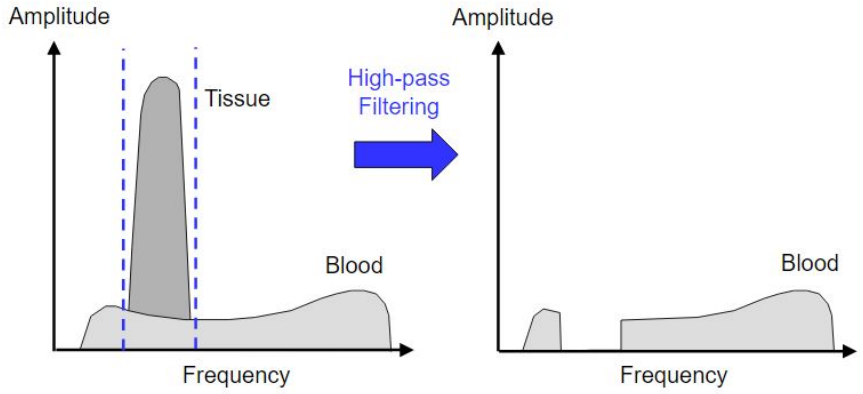

Figure 2.8: Doppler signals from blood can be separated from clutter signals using a high-pass filter to attenuate unwanted signals. Adapted from [23].

For Doppler Ultrasound techniques, the optimal separation between clutter and blood signals can be obtained by using a high-pass filter. The Doppler frequency shift in the signals scattered by rapidly moving blood cells is larger the shift of slowly moving tissue. Therefore, a high-pass filter can be used to attenuate the signals from tissue that have a lower frequency than the cutoff frequency as Figure 2.8 shows. Desired filter properties include high stopband damping to suppress the strong clutter signals, and steep slope between the stopband and the passband to avoid the attenuation of frequencies of interest [22, 21].

The design of a clutter filter is important as it determines whether it is actually blood that is being detected, and thus directly affect the accuracy with which disease is detected [24]. Finite Impulse Response (FIR) filters are the simplest to implement and have many advantages such as computational efficiency, and desirable numeric properties [25]. As the name implies, the impulse response of a FIR filter is of finite length. In which, an output sample can be defined as a linear combination of present and past input samples. We can express this relationship with an equation of the type [25]:

$$y[n] = \sum_{i=0}^{N} b_i \cdot x[n-i] \tag{2.7}$$

where n denotes the temporal sample, i denotes the filter coefficient number, b_i is the value of the i coefficient of the filter, and N is the number of coefficients in the filter. By using a high-pass FIR filter the high-frequency signal from moving blood will pass through while the low-frequency signal from quasi-static tissue will be attenuated. When subtracting two

successive samples, the signal gets attenuated at the points where it changes slowly(low frequencies) and leaves unaffected where the signal varies rapidly (high frequencies) [25].

To illustrate this point Figures 2.9 and 2.10 show the result of a Field II [26, 27] simulation of a coronary artery in two situations: with no tissue motion (Figure 2.9), and with tissue motion (Figure 2.10). In both cases, the blood flow in the coronary arteries is simulated with a cloud of point scatterers moving with velocity (v_x, v_z) = $(5.78, 4.04)$ cm/s. The vessel walls are simulated also with a cloud of point scatterers with 60 dB higher scattering intensity than the blood signal. In the first scenario (Figure 2.9), the blood vessel is static: only the blood moves. In the second scenario (Figure 2.10), the blood vessel moves towards the ultrasound probe in a cyclic pattern.

In Figure 2.9b, we see the spectrum of the signal in the lumen before and after filtering together with the clutter filter response. We see that the tissue signal and the blood signal are easily separable. After filtering, only the blood spectrum remains giving a perfect image of the blood flow Figure 2.9c and Figure 2.9d.
In Figure 2.10b, we see the spectrum of the signal in the lumen for the moving vessel case. We see that the tissue and blood signals are not easily separable: the tissue signal covers the band from -4 to 6 cm/s. After applying the same filter as in the previous case, the tissue signal is not removed.

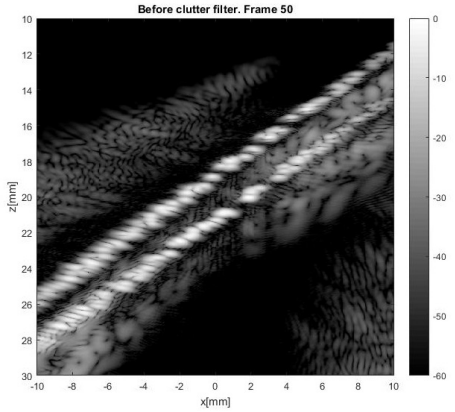

(a) Simulated signal with no tissue motion before clutter filtering.

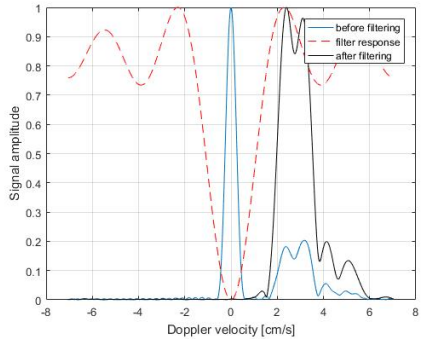

(b) Spectrum of the signal before and after clutter filtering, and filter response.

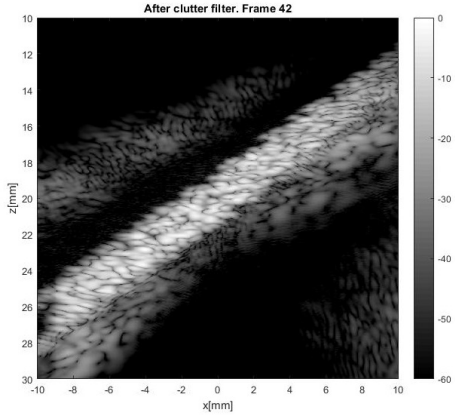

(c) Simulated signal with no tissue motion after clutter filtering.

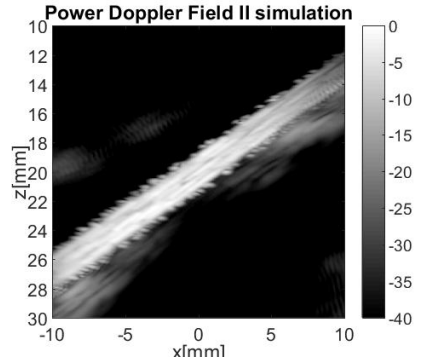

(d) Power Doppler visualization of the blood.

Figure 2.9: Clutter filtering results of simulated signal with no tissue motion.

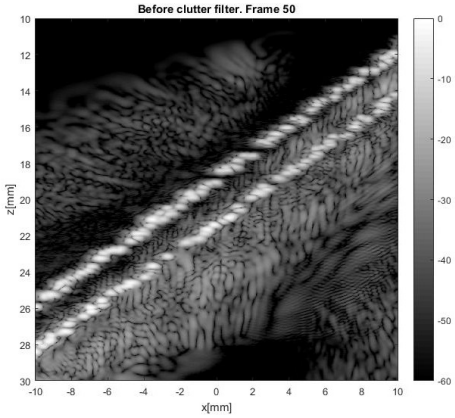

(a) Simulated signal with tissue motion before clutter filtering.

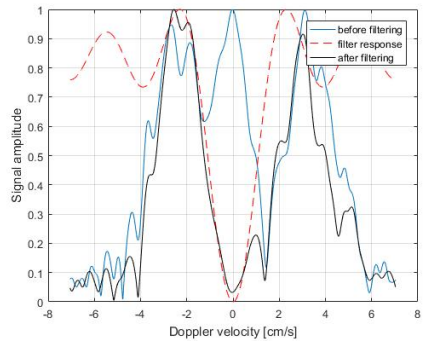

(b) Spectrum of the signal before and after clutter filtering, and filter response.

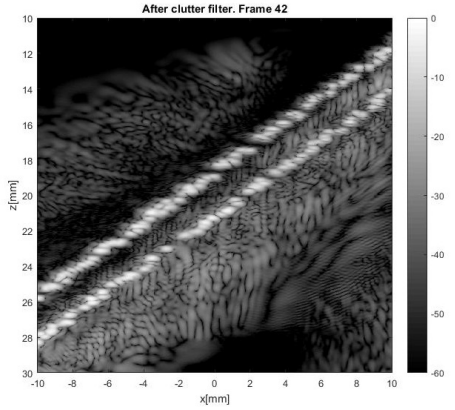

(c) Simulated signal with tissue motion after clutter filtering.

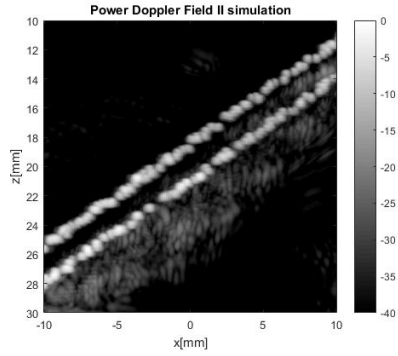

(d) Power Doppler visualization of the blood flow.

Figure 2.10: Clutter filtering results of simulated signal with tissue motion.

2.4 Polyvinyl alcohol

Polyvinyl alcohol (PVA) is a polymer used in many biomedical and pharmaceutical applications due to its desirable characteristics and chemical properties [28]. PVA is non-toxic, not-carcinogenic, easy to process and has a great crystallinity. This makes PVA capable of simulating the ground truth of natural tissue, and is therefore a perfect material for phantom fabrication [29]. PVA can retain more than 20% water within its structure and is a type of hydrogel (a network of polymer chains that are hydrophilic) that has rubber-like properties. PVA phantoms can be formed by cyclic freezing and thawing of an aqueous PVA solution composed of water and PVA powder. The freeze-thaw (F-T) process causes

the PVA mixture to cross-link through hydrogen bonding with hydroxyl groups on PVA molecules which result in a PVA cryogel [28].
The crystalline nature of PVA cryogel (clearness) is a desired characteristic for imaging purposes, and it is related to the concentration of PVA in solution, freezing time, and the thawing time [29]. PVA phantoms may be designed with different physical properties such as sample velocity and elasticity, by not only varying the number of F-T cycles in the fabrication process but also the length of each F-T cycle [28].

2.5 Measurement Methods

Tissue mechanical properties can be characterized using different measurement methods. Ultrasound can be used to estimate properties such as tissue stiffness and velocity. For this project, the elastic parameters of PVA cryogel is characterized.

2.5.1 Estimation of the Velocity of Longitudinal Waves

The discrete frequency method is used for measuring the longitudinal wave velocity of a sample material. This method can be implemented using either one or two transducers. When two transducers are used, one serves as a transmitter and the other one as a receiver. Both transducers are mounted co-axially in a water tank where water is used as the reference medium. A toneburst is sent with normal incidence to the sample to be measured. The longitudinal velocity of the sample v_l can then be estimated with Equation (2.8) by measuring the difference in time-of-flight (TOF) between the signal with and without the sample in place:

$$v_l = \frac{v_w}{1 - \frac{\Delta t v_w}{d}} \tag{2.8}$$

where v_w is the velocity of the reference medium, d is the sample thickness and Δt is the TOF received at the receiver [30].

2.5.2 Estimation of the Velocity of Shear Waves

Shear Wave Elastography (SWE) uses ultrasound to estimate material properties of tissue, such as tissue stiffness. It relies on the generation and measurement of shear waves in a focal region within the tissue. This shear wave can be generated by direct physical contact with the use of an external vibrator, or internally within the tissue by using the acoustic radiation force [31, 10].

An acoustic radiation force is generated by an ultrasound beam and is directed in the direction of the wave propagation [10]. Acoustic Radiation Force Imaging (ARFI) uses a high-output ultrasound beam to displace a region of tissue, and imaging beams to monitor the displacement in the focal region. Shear waves are generated at arbitrary locations by focusing a pushing beam. The pushing beam, also called pushing pulse, produces a radiation force which displaces tissue in the focal point and generates the shear waves. The magnitude of the force is highest in the focal zone and increases with overall output power.

To generate each line of ARFI imaging it requires at least three ultrasound pulses; a pushing pulse and two imaging pulses. A first imaging beam is sent to record the position of the tissue in its resting position, and a second imaging beam is sent immediately after the pushing beam to monitor the position of the tissue while being displaced. One disadvantage of regular ARFI method is that shear waves are being generated from a single focal point limiting the region covered by the shear waves [10].

The Doppler effect occurs due to the relative motion between the blood and the transducer. The transmitted frequency as experienced by the blood is dependent on whether the blood is stationary, moving towards the transducer or away from the transducer at the time the transmitted sound waves hit the blood. The transducer then detects the backscattered signals coming towards the transducer. Due to the motion of blood, the scattered Doppler frequency is shifted again [10]. The Doppler shift can be estimated by:

$$f_d = f_r - f_t = \frac{2 f_t v \cos\theta}{c} \tag{2.9}$$

where c is the sound speed in tissue, v is the velocity of blood, θ is the angle between the path of the ultrasound beam and the direction of the blood flow, and f_t and f_r are the transmitted and received frequency; respectively [10]. If the angle θ is known, it is possible to use the Doppler shift frequency to estimate the velocity of the blood by rearranging Equation (2.9):

$$v = \frac{c f_d}{2 f_t \cos\theta} \tag{2.10}$$

Doppler Tissue Imaging (DTI) is used to measure tissue displacement using the Doppler effect. A positive frequency shift will occur if the tissue is moving towards the receiver [21, 31]:

$$f_d = f_0 \frac{c + v}{c} \tag{2.11}$$

Considering the two-way Doppler shift for a scatterer, acting both as a transmitter and a receiver, the following relation for positive velocity towards the transducer can be derived [31, 21]:

$$f_d = f_0 \frac{c + v}{c - v} \tag{2.12}$$

where f_d is the frequency detected by the receiver, v is the velocity of the tissue towards the receiver, and c is the speed of sound in the medium [31, 21].

Using a pulsed wave acquisition scheme, the signal received from regions of moving tissue can also be seen as a phase-shifted signal which can be used to measure the velocity [31]. Given that the frequency shift is smaller than the central frequency, $\Delta f \ll f_0$, and that the velocity is in the axial direction, the phase shift can be found through autocorrelation [21]:

$$v = \frac{\angle R_1 PRF c}{4\pi f_0} \tag{2.13}$$

where PRF is the pulse repetition frequency of the imaging sequences and R_1 is computed by the summation of the complex conjugate multiplication of consecutive frames [31]:

$$R_1 = \sum_{k=1}^{N} z_k . z_{k+1}^{*} \tag{2.14}$$

$\angle R_1$ is the angle of these complex values and represents the phase-shift between individual frames [31].

Figure 2.11 shows a schematic representation of SWE using ARFI and TDI:

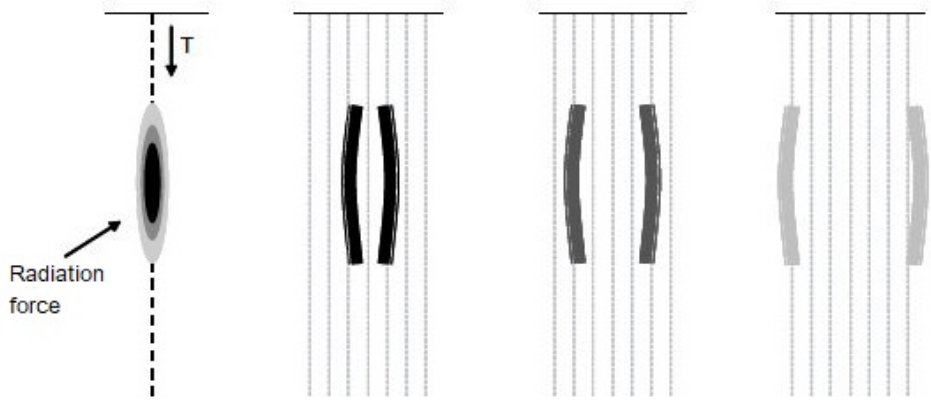

Figure 2.11: A high-output beam produces a radiation force which displaces tissue in the focal region, producing shear waves which propagate in 3D. High-frame-rate imaging techniques such as TDI are used to track the tissue displacement caused by the shear wave. Adapted from [10].

2.6 3D Positioning System

In order to simulate the ground-truth of coronary blood flow, a 3D - positioning system can be used. In a three-dimensional space, an object has 6 degrees of freedom. It means that an object may either rotate about or translate along any of the 3 axes (XYZ).

The 3D positioning robot system consists of 3 linear translation stage motors for position control in more than one direction. A linear stage is a component of a precise motion system which exhibits only one degree of freedom and is used to restrict an object to a single translation axis of motion. All linear stages consist of a platform that moves in a straight line relative to a fixed base. The position of the moving platform relative to the base is controlled by a DC motor with a linear encoder. A linear encoder is a sensor with a scale that encodes position. The DC motor is used to measure the position of the stage relative to the scale and report this to the motor controller. This allows the motion controller to reliably and repeatably move the stage to set positions [32].

Figure 2.12 illustrates the 3D positioning system axes setup used for this project. An XYZ linear stage combination consisting of 3 linear stages is used to control the motion in each axis.

Figure 2.12: XYZ Linear stage combination setup an axes direction as described above adapted from [33].

As it can be seen in Figure 2.12, the 3 linear stages are mounted to each other such that the axes of motion are orthogonal [32]:

- X: linear motion in a positioning direction
- Y: linear motion perpendicular to the positioning direction
- Z: vertical linear movement

The main of the objective of the 3D positioning system is to simulate a 3D periodic signal s as a function of time t as a collection of points in space:

$$s(t) = A\sin(2\pi ft + \phi) \tag{2.15}$$

where A is the signal amplitude given in meters, ϕ is the signal phase given in radians, and f is the frequency in Hz.

This set of parameters is used to calculate the total trajectory and simulate the ground-truth of blood flow through the coronary arteries. Since the periodic signal is to be reconstructed in the 3D space, the signal parameters are given as a set of vectors for each axis (XYZ).

$$\vec{A} = \begin{bmatrix} A_x \\ A_y \\ A_z \end{bmatrix}; \quad \vec{\phi} = \begin{bmatrix} \phi_x \\ \phi_y \\ \phi_z \end{bmatrix}; \quad t(n) = \frac{n}{fN}, n \in [0, N] \tag{2.16}$$

Where $\vec{A}$ and $\vec{\phi}$ are the signal amplitude and phase vectors, respectively. The size of $t(n)$ is given by the number of points N, which are to be simulated. The position of the robot is a point in space along the total trajectory path that changes with time. Equation (2.17) is used to calculate the next position ($\vec{r_{c+1}}$) in the trajectory given the current position $\vec{r_c} = \begin{bmatrix} x_c & y_c & z_c \end{bmatrix}^t$ for all axes, and the signal parameters as in Equation (2.16):

$$\vec{r_{c+1}} = \vec{r_c} + \vec{A}\sin(2\pi\vec{f}t + \vec{\phi}) \tag{2.17}$$

where the current position is the actual position of the linear stage relative to the scale, and is given in mm. Unit conversion to radians and to millimeters is made prior to the calculation of the robot trajectory. The total robot trajectory for all points N in space is calculated and given in the matrix form:

$$\vec{r_i} = \begin{bmatrix} \vec{x} \\ \vec{y} \\ \vec{z} \end{bmatrix} = \begin{bmatrix} x_0 & x_1 & x_2 & \dots & x_n \\ y_0 & y_1 & y_2 & \dots & y_n \\ z_0 & z_1 & z_2 & \dots & z_n \end{bmatrix}, i \in [0, n] \tag{2.18}$$

where the vector $\vec{r_0} = \begin{bmatrix} x_0 & y_0 & z_0 \end{bmatrix}^t$ is the initial stage position at $(t = 0)$, and the dimension of the trajectory matrix is given by the number of points and the number of axes, in this case: 3xN.

Chapter 3

Materials and Methods

This chapter describes the fabrication, and characterization process of the PVA phantoms. Also, a detailed description of the user interface programmed to control the 3D positioning system is given in Section 3.4. Finally, a description of the experimental setup for coronary blood flow imaging is given.

3.1 Mold Fabrication

The molds used for the fabrication of all PVA phantoms were designed using Autodesk Inventor 3D CAD Software. They were all fabricated using a Lulzbot TAZ 5 3D printer seen in Figure 3.1, and Red NinjaFlex filament. NinjaFlex was used for printing all molds since it has good elasticity and shape memory, which is a necessity under the F-T cycles all phantoms must undergo.

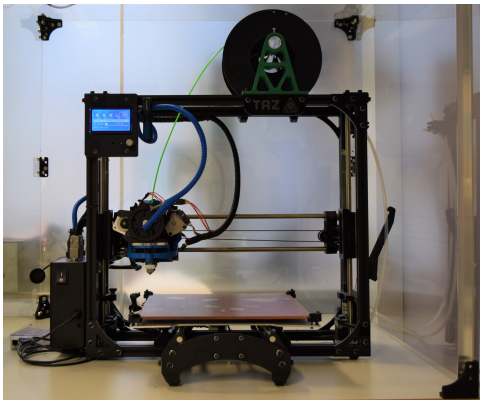

Figure 3.1: 3D printer used for the fabrication of the molds.

Figure 3.2a shows the PVA sample molds with an outer geometry of 40 mm height, 40

mm width and 70 mm length; and an inner diameter of 30 mm height, 30 mm width and 50 mm length. In addition to the molds for the PVA samples, a mold for the heart ventricle phantom with a volume of approximately 2.5 dL was previously fabricated. Figure 3.2b shows the ventricle mold.

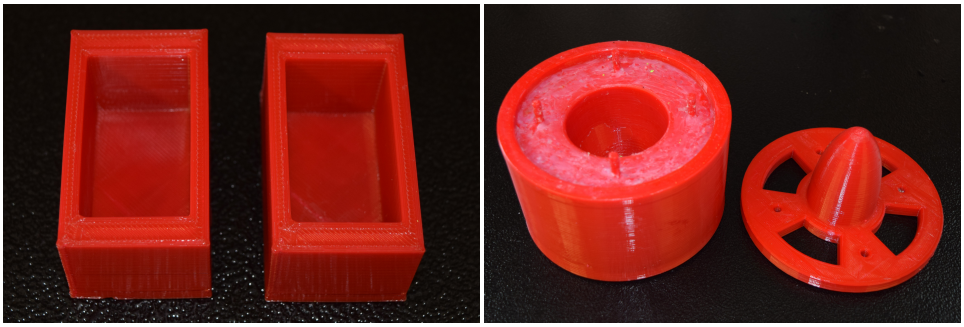

(a) PVA sample rectangular molds. **(b)** Heart ventricle phantom mold.

Figure 3.2: Different molds used for PVA phantom fabrication

3.2 Phantom Fabrication

All phantom fabrication processes were done using fully hydrolyzed PVA powder from Sigma-Aldrich. All molds were measured, and the total volume required for the fabrication process was calculated.

3.2.1 General Fabrication Process

An aqueous solution of PVA was prepared by dissolving a weighed amount of PVA powder in distilled water in a 500mL beaker glass. The composition of the solution was 10% PVA powder and 90% deionized water. A magnetic stirrer (Heidolph MR Hei-Standard) and a magnetic bar were used to achieve a more homogeneous mixture. The solution was then placed in an orbital shaking water bath (Grant OLS200) and heated to 80 °C. The beaker glass was covered with an aluminum foil in order to avoid water evaporation during the heating process. A thermometer (Omega HH147RS-232 Data Logger) was used during the heating process to control the temperature at all times. After achieving the desired temperature, and getting a nearly transparent solution, the mixture was removed from the water bath and placed back onto the magnetic stirrer. The mixture was stirred once again at $100 - 200$ rpm until the temperature decreased to approximately 30 °C. This was done in order to achieve a more homogeneous solution before it was poured into the molds. The PVA aqueous solution was then allowed to cool at room temperature in order to remove the bubbles generated by the stirring process. After all the bubbles were removed, the PVA solution was subjected to multiple freeze–thaw cycles.

The F-T temperatures were controlled by a programmable temperature controller and a commercial freezer. The temperature range for one F-T cycle was from -23 °C to 23 °C,

starting always with a freeze cycle.

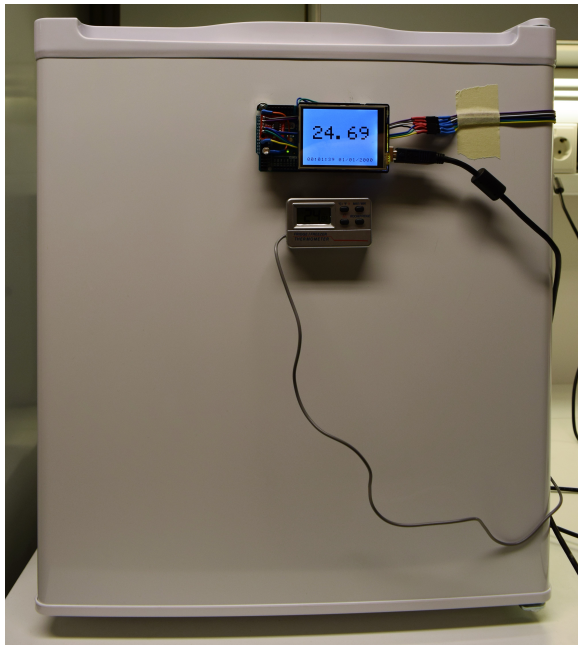

Figure 3.3: Freezing and thawing temperatures were controlled using a commercial freezer and a temperature controller.

3.2.2 Block Samples

The fabrication process took place on two dates, and two sets with two PVA samples were fabricated.

At the first fabrication date, one set of two PVA samples were fabricated using the molds with dimensions as described in Section 3.1, and shown in Figure 3.2a. It was required a total of 90 mL PVA solution since the volume of each sample mold was of 45 mL. In order to simplify the mixing ratios and to have some leeway in case of material losses, there was mixed a total of 100 mL PVA aqueous solution: 10g fully hydrolyzed PVA powder and 90g degassed and deionized water. The fabrication process was as described in Section 3.2.1. The PVA samples were subjected to a total of 5 F-T cycles with a duration of 12 hours freezing and 12 hours thawing.

For the second fabrication date, the same molds as before were used. As the molds dimensions were the same, there was also mixed a total of 100 mL solution: 10g fully hydrolyzed PVA powder and 90g degassed and deionized water. The general fabrication process as described in 3.2.1 was also used in this case, but the duration of the F-T cycle was different than in the first fabrication date. These PVA samples were subjected to a total of 5 F-T cycles with a duration of 24 hours freezing and 24 hours thawing.

Figure 3.4 shows the sample results from the second fabrication date after being subjected to multiple F-T cycles.

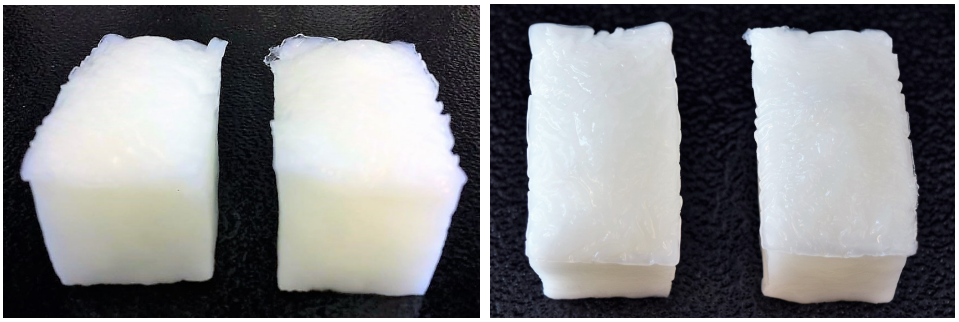

Figure 3.4: PVA samples after multiple F-T cycles.

3.2.3 Heart Ventricle and Coronary Arteries

For the fabrication of the PVA coronary arteries, clear plastic straws were used as the outer mold. The clear plastic straws were found to be suitable as molds due to their size, and capacity to resist pressure changes during the F-T cycles. The inner artery wall was created using knitting needles with an outer diameter of 3mm.

All coronary artery phantoms were fabricated following the general fabrication process described in Section 3.2.1. The size of the outer mold was 5 mm diameter and 10 cm length. For the fabrication of each artery, a knitting needle was placed inside the plastic straw and held in place with a plunger seal from a 5 mm syringe, one on each side. The PVA solution was poured into the plastic straws using a syringe to achieve accuracy and avoid material losses. Some coronary arteries were subjected to multiple F-T cycles with a duration of 12h, while others to a duration of 24h. This was in order to study the differences in the properties of the PVA coronary artery phantoms.

Figure 3.5 shows the result of different coronary artery phantoms with different F-T cycles and cycles duration. The appropriate phantom elasticity and strength for healthy arteries were found after 2 F-T cycles with a duration of 24h each. For the fabrication of the healthy coronary phantoms, the molds were not removed before all F-T cycles required were completed. This was done to avoid the phantoms to deform during the F-T cycles. Otherwise, the phantoms would have deformed and their structure would have changed.

The physical properties of PVA coronary phantoms such as their strength can be increased by increasing F-T cycles. After removing the phantoms from the molds, the flow inlets and microfluidic plastic tubes were placed without damaging the phantom wall.

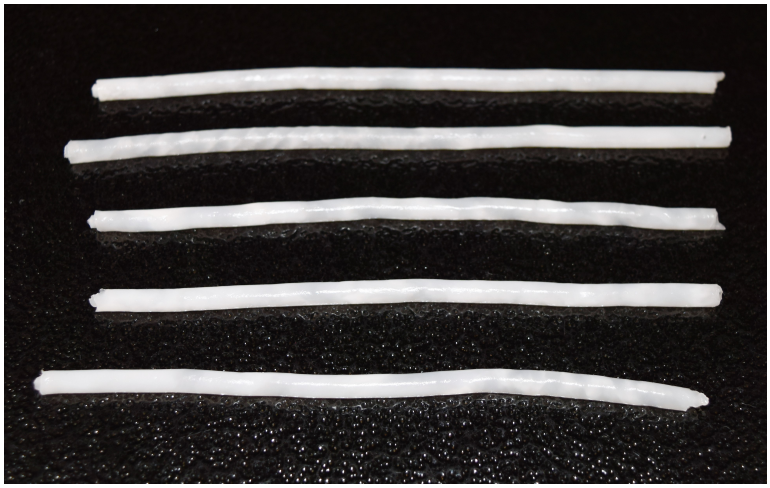

Figure 3.5: PVA coronary artery phantoms with different F-T cycles

For the fabrication of the heart ventricle, a two-piece mold as shown in Figure 3.2b was used. A total of 3 dL aqueous PVA solution was used to fill the mold following the general fabrication process previously described. The PVA heart ventricle phantom was subjected to 2 F-T cycles with a duration of 24h before it was removed from the molds. The result from the fabrication process and the shape of the ventricle phantom can be seen in Figure 3.6.

3.2.4 Integration of ventricle and coronary phantoms

After the fabrication process of the heart ventricle and the coronary arteries had been completed, two coronary arteries were glued to the ventricles surface as it can be seen in Figure 3.6. For this, a new PVA aqueous solution was fabricated to glue the phantoms together. Instead of allowing the mixture to cool down at room temperature, it was placed in the freezer just until it had started to freeze. This was necessary in order to decrease the temperature as much as possible for the mixture to become denser and sticky. When the PVA solution was sticky enough, the coronary arteries were placed around the ventricle and the mixture was then poured over both phantoms. The whole system was then subjected to one F-T cycle of 24h. The gluing process was repeated at least 3 times until the coronary arteries were completely attached to the surface of the ventricle.
Figure 3.6 shows the results of the complete system.

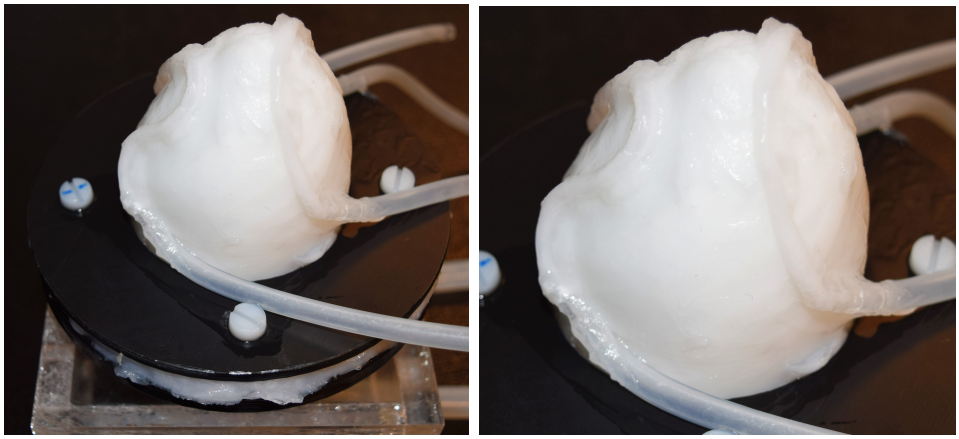

Figure 3.6: Coronary arteries with flow inlets and outlets wrapped around the PVA heart ventricle phantom.

3.3 Characterization of the PVA samples

3.3.1 Longitudinal Velocity

The longitudinal velocity of all the PVA samples was characterized using a tank system. The measuring system as Figure 3.8 shows, consisted of a small water tank with two mounted immersion transducers (C309-SU) with an operating frequency of 5 MHz. One of the ultrasonic transducers was connected to a signal generator and worked as a pulse transmitter, while the other one was connected to an oscilloscope and worked as a pulse receiver.

A PVA sample with known thickness was placed between the two transducers and held in place using a quadratic sample holder. The mini tank was filled with enough degassed and ionized water to cover both transducers, and it was also used as the host medium. The transmitter was connected to channel one of Agilent 33522 arbitrary waveform generator, which was used for all measurements. A sine wave burst with an amplitude of 10 Vpp, 5 MHz frequency, 5 cycles, and 10 ms burst period was used as the general setting for all measurements. The receiver was connected to an oscilloscope (LeCroy WaveSurfer 42Xs-A), and a trigger signal to the sync the output of the signal generator. Bayonet Neill–Concelman (BNC) connectors were used for connecting the different electrical components.

Figure 3.7 shows a schematic representation of the system setup for the longitudinal velocity measurement.

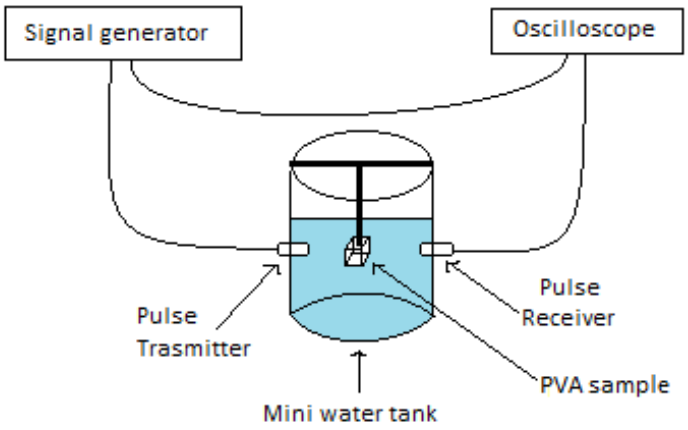

Figure 3.7: Schematic representation of the longitudinal velocity measurement system setup taken from [34].

The longitudinal velocity from all samples was estimated as described in Section 2.5.1. To ensure that the sample was correctly oriented and there was a full signal transmission, both sample and holder were rotated until the signal amplitude displayed reached its highest value. The mean V_{rms} and delay values from the transmitted signal with and without a PVA sample displayed on the oscilloscope, were recorded and downloaded using a USB drive. Figure 3.8 shows the actual system setup with all components used to measure the longitudinal velocity in PVA phantoms:

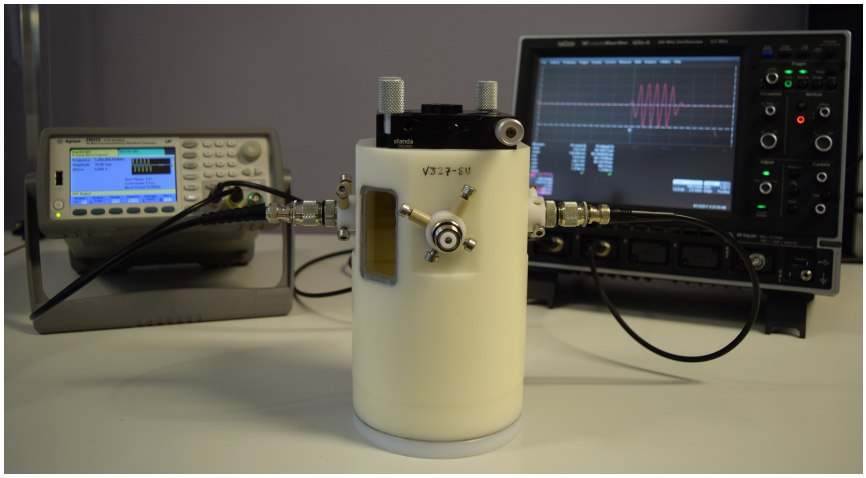

Figure 3.8: System setup for measuring the longitudinal velocity in PVA phantoms.

A script written in MATLAB R2016b (Appendix D) was used to implement Equation

(2.8) and for further signal analysis. The same measuring setup was used and the process was repeated for all PVA samples.
A complete equipment list used in the measurements can be found in Appendix B.2.

3.3.2 Shear Wave Velocity

All shear wave velocity measurements in all PVA samples were done in a Verasonics Vantage 256 ultrasound research system using a L11−4v linear array probe with 128 channels. An example script provided by Verasonics for shear wave imaging was used to control the imaging sequences. The same setup was used for all measurements with the central frequency (f_0) of 4.8 MHz, imaging-PRF of 10 kHz and push-PRF of 5 kHz. The length of the push pulses was 100μs, and a max voltage of 35 V.

Beamformed IQ-data was stored for a region with depth ranging from 9.6 to 41.6 mm, and a width from −16 to 16 mm relative to the center of the transducer. Shear wave propagation was generated in real time and visualized in B-mode, while 2D velocity maps were generated in post-processing.

The main SWE technique used in all measurements was ARFI, as described in Section 2.5.2. The shear waves were imaged using TDI, with 50 active push elements and 781 push cycles. The imaged data was beamformed and complex-demodulated before being stored as IQ-data. To see the movement over time, the mean of the TDI over depth was found in every frame and mapped as lateral position and time. The shear wave velocity for each PVA sample was found by manually creating a line at the depth of the ARFI focal point and calculating the lateral displacement of the shear wave over time.

3.4 Robot control

This section describes the implementation of the user interface for the robot control system described in Section 2.6. It also contains the external interfaces requirements involving the user, hardware, software and communication interfaces. The complete program for the robot control system was written using MATLAB R2016b, and it has been attached with the name ”Robot Code” as a supplementary file.

3.4.1 System Overview

The 3D positioning robot system consists of a combination of three high-precision linear translation stage motors by Physik Instrumente. The XYZ-axis combination consists of M-521(5IM) and M-521(5IS) precision stages, for x-axis and y-axis respectively; and M-531(5IS) precision stage for the z-axis. The XY-axis is horizontally aligned and with a travel range of 204 mm, while the z-axis is mounted vertically and has a travel range of 306 mm.
The system motors are DC motors with pulse-width modulation (PWM) control with an operating voltage of 24 V, in combination with directly measuring linear encoder for high

resolution and repeatability. In addition, it has a sensor resolution of 0.02 μm and a minimum incremental motion of 0.1 μm. The communication interface for the robot consists of Native commands from the Physik Instrumente General Command Set (GCS) for the C-863 Mercury^{TM} DC-motor servo-controller.

3.4.2 System Requirements

The following system requirements should be met in order to ensure the reliability of the system:

- Usability: The user should be able to operate, learn, and control the system without any previous knowledge about programming or robot control.
- Maintainability: The system should facilitate the maintenance, implementation or any necessary modifications to be made to the system.
- Availability: The system should be up and running as long as there are no system constraints. The application should also be able to establish a wireless and serial connection with the robot.
- Portability: The application should be able to be run from different operating systems.

Hardware Requirements

For the user to be able to operate the system, the following hardware requirements should be met:

- USB-port: for support of external platforms.
- Serial-port: for support of a serial communication interface.
- Wireless access: for support of wireless local area networking.
- A computer that supports MATLAB R2016b.

Software Requirements

In addition to the hardware requirements, the system is dependent on the program MATLAB R2016b to be installed on the computer in order for the user to run the application and control the system.

User Requirements

The program should allow the user to control the application without having a total understanding of the implementation of the code, and the internal functionality or structure of the application:

- Connect and disconnect from the robot.

- Choose the connection type.
- Edit signal parameters as long as the values are valid and not constrained.
- Start, pause and completely stop the robot given a trajectory.
- Control the relative movement of each axis with a given step and direction.
- Move the robot to the origin.
- Get a clear warning of any deviation in the robot behavior.
- Get information about the robot trajectory.
- Get a warning about boundaries and constraints.
- Use the emergency button to interrupt the trajectory if necessary.
- Edit the software boundaries.

Assumptions

The system assumes that the users have the necessary knowledge and skill with using computers and computer software.

3.4.3 System Design

The robot control system is launched from the main function called robControl (see attachment). The system is divided into two parts: the Physik Instrumente object which is initiated and controlled by a robot object; and the graphical user interface (GUI) which provides point-and-click control of the application eliminating the need to learn a programming language or terminal commands in order to run the application.

The robot object contains information related to the robot properties and communication. Including functions for connection setup, send and receive commands to and from the robot, etc. The type commands used to communicate with the 3D positioning robot from Physik Instrumente was the native ASCII (American Standard Code for Information Interchange) command set, which is understood by Mercury^{TM} firmware directly. ASCII assigns a number of electrical signals to each number and letter of the alphabet. In this manner, alphanumeric information can be transmitted between machines in a series of binary numbers [32].

All motion of the connected motors and mechanical stages is also software controlled. Table 3.1 contains a list of the commands used to control the robot and their function:

Command	Function	Description
DHn	Define Home	Defines the current motor position as n
FEn	Find Egde	Searches for the reference (origin) position in n direction
GH	Go Home	Causes the motor to move to the currently defined zero position
MAn	Move Absolute	Starts a move to absolute position n
MRn	Move Relative	Starts a move of relative distance of n steps from the current position
TP	Tell Position	Reports the absolute position of the motor
TS	Tell Status	Reports the status of the system, its motion and limit switch states

Table 3.1: Base commands used to control the robot.

3.4.4 Users Manual

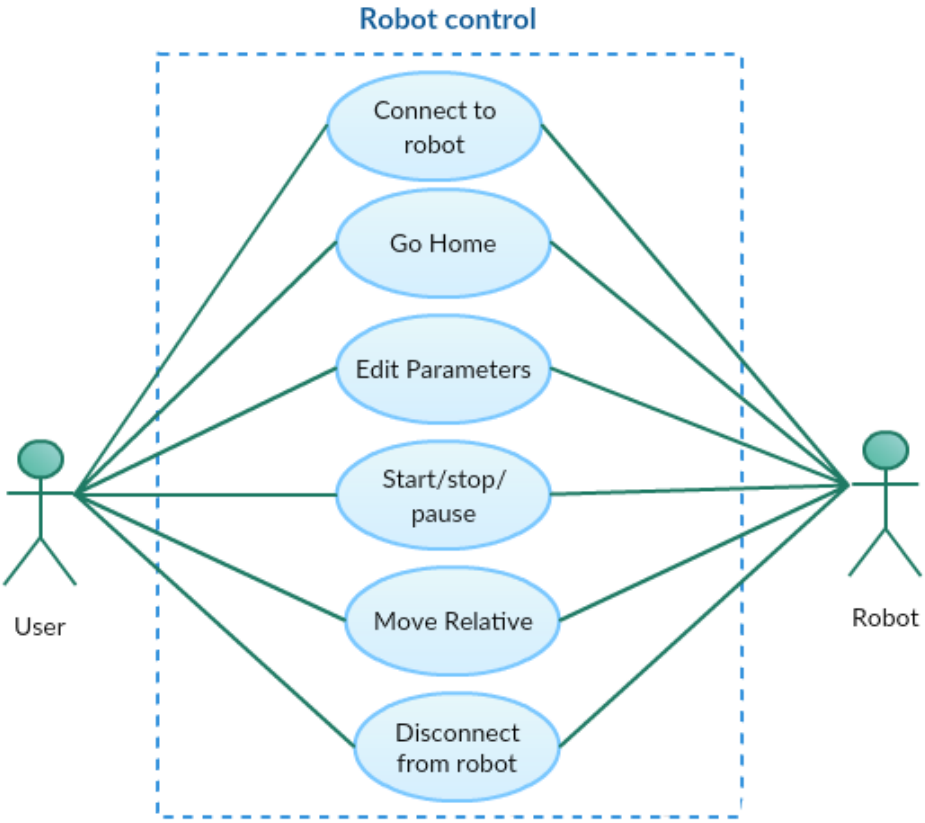

Figure 3.9: Use case diagram for robot control

Primary Actor:

User

Brief:

The user starts the program and the programs GUI is launched. The connect button is pushed and the connection type is chosen. After the connection is successfully initialized, the robot is ready to start receiving commands. The user can then chooses between going home, controlling the relative robot movement in either one or all three directions or starting a trajectory with edited parameters. The user can always disconnect from the robot as long as a command is not being executed and the robot is not moving. Buttons are enabled or disabled during program execution to ensure proper robot behavior.

Minimal Guarantees:

The user is able to connect and disconnect from the robot, and the robot responds to at least one command sent.

Success Guarantees:

The user is able to connect and disconnect from the robot, and the robot movement response is equivalent to the command sent.

Preconditions:

The robot is connected and turned on, the connection ports are available.

Triggers:

The user runs the program, the GUI for robot control is launched and the user pushes some GUI button.

Basic Flow:

1. The system is running and the GUI for robot movement control is launched.
2. The user pushes the connect button, and a dialog box lets the user choose the connection type.
3. The user chooses connection type: wifi or USB, the robot object is initialized with the port that corresponds to the connection type, and the connection is made.
4. The user can choose to go home, move relative from the initial position by a chosen step size, or to initiate a periodic movement trajectory by editing the parameters.
    - 4.1 Go home button is pushed: The robot initiates movement towards the center of all three axes, reset all previous commands, overwrites software settings and defines the origin as the initial position.
    - 4.2 Step size, direction (positive or negative), and the axis(XYZ-axis) are chosen before starting the relative movement. Buttons are pushed, commands are sent to the robot and the robot moves to the new position.

4.3 To generate a periodic movement trajectory, parameters such as amplitude, phase for all three axes and the number of points are edited.

The start button is enabled and the trajectory is calculated as long as all the parameters are valid.

The start button is pushed and the periodic movement is initiated. The robot moves to each point in the trajectory and continues until the pause or stop button is pushed.

5. The user pushes the disconnect button, the command is sent and the connection is terminated.

3.5 Experimental setup for coronary blood flow

Verasonics Vantage 256 Ultrasound research system for all measurements using a L12-3v broadband linear array probe. The phantoms used for the final setup were the ventricle and the coronary arteries previously fabricated and described in Section 3.2. The ultrasound probe was moved with the 3D positioning system previously implemented, and as described in Section 3.4. Water was used as the host medium for all measurements.

The method used for image acquisition and recording of the flow in the coronary arteries in all simulations, was the coherent plane wave compound imaging method as described in Section 2.2. The script used for the plane wave imaging process of the coronary arteries was written in MATLAB and has been attached as complementary material in the coronary artery imaging file. There were used 128 channels for the image acquisition with a working central frequency of 7.81 MHz, 7 plane waves and 100 frames were recorded.

The ventricle phantom was placed in a sample holder (see Figure 3.10), and connected to a pulsatile flow pump and with a pressure regulator chamber as shown in Figure 3.10. The phantom was then placed on the bottom of the water tank. The water tank was filled with deionized water. The pressure regulator chamber was used as bubble trap from inside the plastic tubes connecting the pulsatile water pump to the ventricle. The pulsating water pump was used to control the movement of the ventricle by pumping water into its cavity, causing the ventricle to expand and contract.

A continuous flow water micro-pump was connected to the coronary artery phantoms using the plastic tubes previously attached to the coronary arteries.

A solution of water and orgasol powder (Orgasol powder Type 3502 D NAT 1) was used to simulate the continuous flow through the coronary arteries using the micro water pump. The solution was stirred at 200 rpm using a magnetic stirrer to achieve an equal particle dispersion through the arteries and to prevent the particles from blocking the tubes.

Figure 3.10 shows a close up image of the real experimental setup:

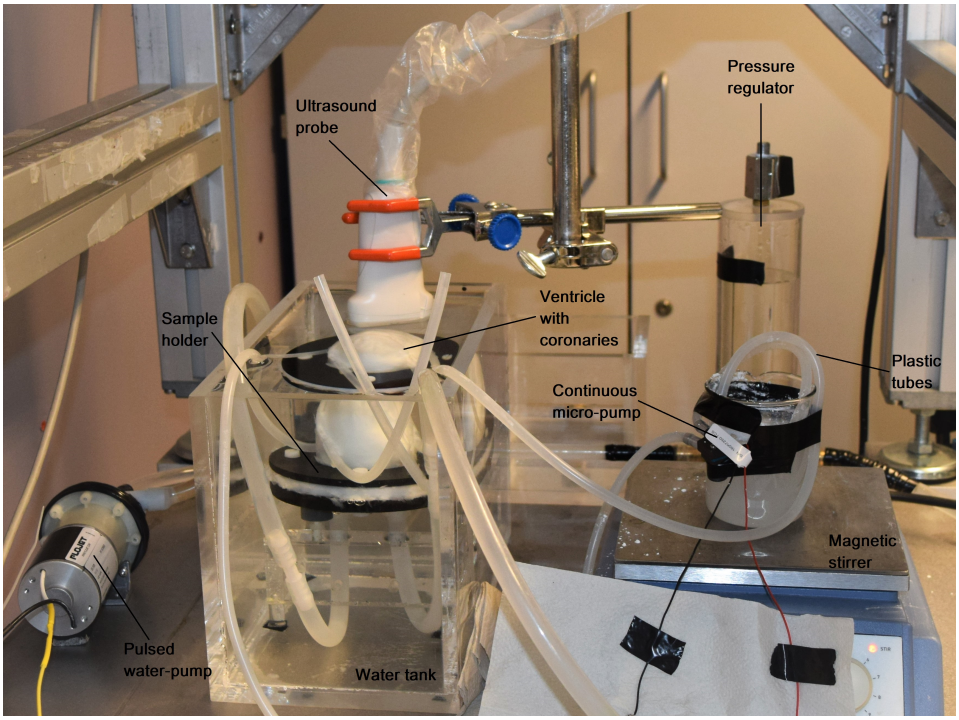

Figure 3.10: Real footage of the experimental setup for coronary artery blood flow.

The pulsating water pump system allowed to set up a pulsating flow with a known rate of 40 bpm. It was also possible to regulate the voltage applied to the pump, and hence the change in the flow velocity, which was measured as a percentage ($\%$) of the maximum voltage (V_{max}) of 12V that can be applied to the pump.

Figure 3.11 illustrates a schematic representation of the final experimental setup:

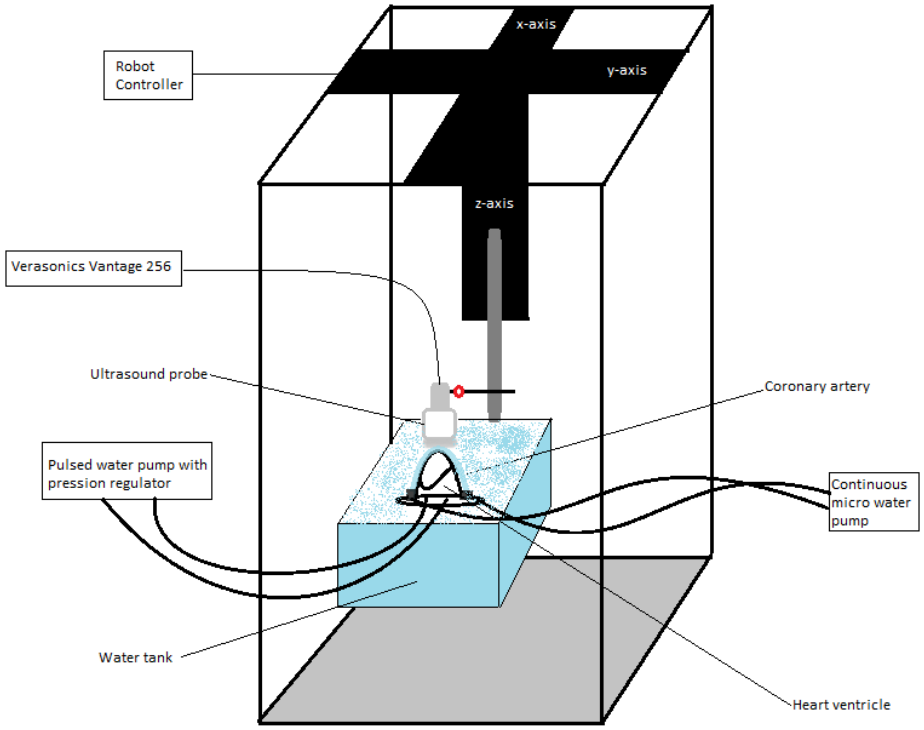

Figure 3.11: Experimental setup for coronary artery blood flow.

The robot was connected to an Arduino Mega 2560 which was used as an external platform for robot control. The Arduino had 4 serial ports, but only two of them were used. One of the serial ports was connected to the computer over a USB-port, and the other one was connected to the robot over an RS-232 interface. The Arduino was used to forward all the ASCII formatted strings (commands) to and from the robot. A trigger out was implemented to send a trigger to the Verasonics 256 for the imaging process to start. In addition to the trigger signal, an emergency stop button was also implemented to stop the robot immediately if necessary. The main objective of the button is to stop the robot by blocking the message forwarding process when the emergency button is pressed and remain blocked until it is pressed again.

The trigger and the ultrasound probe were connected to the ultrasound research system. The ultrasound probe was placed on a vertical holder attached to the Z-axis using a clamp. It was then moved using the robot control system until it was placed just above the coronary artery to be imaged. The software boundaries for the robot were modified to match the surface geometry of the water tank. This was done in order to constrain the range of motion of the robot and to prevent collision accidents with the rest of the system components.

The first three experiments were done using the ventricle pulsatile water pump, and other three experiments using the robot.

3.5.1 Ventricle Motion Using the Pulsatile-pump System

The first experiment was done with the ventricle at rest (no amplitude and pulse), the second one with an amplitude of 40% of the max voltage and a pulse rate of 40 bpm. For the third experiment, the ventricle motion was increased and simulated using an amplitude of 60% of V_{max}, and a pulse rate of 70 bpm. Three different PRF were used for the acquisition of the data: 10000 Hz, 5000 Hz and 2000 Hz. The experiments were done in a decreasing order: from the highest to the lowest PRF value.

Table 3.2 contains an overview of the experiments using the pulsatile water pump to create the motion of the ventricle:

PRF	10000 [Hz]		5000 [Hz]		2000 [Hz]	
Simulation	Amplitude [%]	Pulse [bpm]	Amplitude [%]	Pulse [bpm]	Amplitude [%]	Pulse [bpm]
1	0	0	0	0	0	0
2	40	40	40	40	40	40
3	60	70	60	70	60	70

Table 3.2: Signal values used to simulate the ventricle motion using the pulsatile pump system.

3.5.2 Ventricle Motion Using the Robot

Another three coronary blood flow signal experiments were conducted using the robot. The CPWI datasets were also acquired and recorded using the same script as before. All three experiments were done using 100 points and with a signal amplitude in the z-axis of 0.5 mm, 1.5 mm, 2.5 mm, for the first, second and third experiment respectively. The x- and y-axis were constrained under all measurements by a signal amplitude of zero. By doing this, a linear vertical motion of the ultrasound probe was generated only along the z-axis simulating the pulsation of the ventricle in one direction. The signal phase was also zero for all xyz axes.

Table 3.3 contains an overview of the signal simulations using the robot:

Simulation	Amplitude [mm]	Number of points [ ]
1	0.5	100
2	1.5	100
3	2.5	100

Table 3.3: Signal values used to simulate the ventricle motion using the robot.

The acquired data for all experiments was stored, and clutter filtered in post-processing.

3.5.3 Clutter Filter Design Values

The filter coefficients used in the design of the clutter filter are given by the coefficient vector:

$$\begin{aligned}\vec{b} = [&-0.0995 - 0.1080 - 0.1144 - 0.1184 \\ &0.8803 - 0.1184 - 0.1144 - 0.1080 - 0.0995]\end{aligned} \tag{3.1}$$

and the maximum velocity to be measured can be calculated using Equation 3.2:

$$v_{max} = \frac{\mathrm{PRF} \cdot c_0}{4 \cdot \mathrm{numberofplanewaves} \cdot f_0} \tag{3.2}$$

with the following values:

$$\begin{aligned} c_0 &= 1540 \ \ \mathrm{m/s} \\ f_0 &= 7.8 \ \ \mathrm{MHz} \\ \mathrm{numberofplanewaves} &= 7 \end{aligned}$$

where c_0 is the sound speed, f_0 is the transmitted frequency, and the PRF is the same as for the acquired data.

Figures 3.12 shows the filter spectra with a corresponding PRF of 1000 Hz:

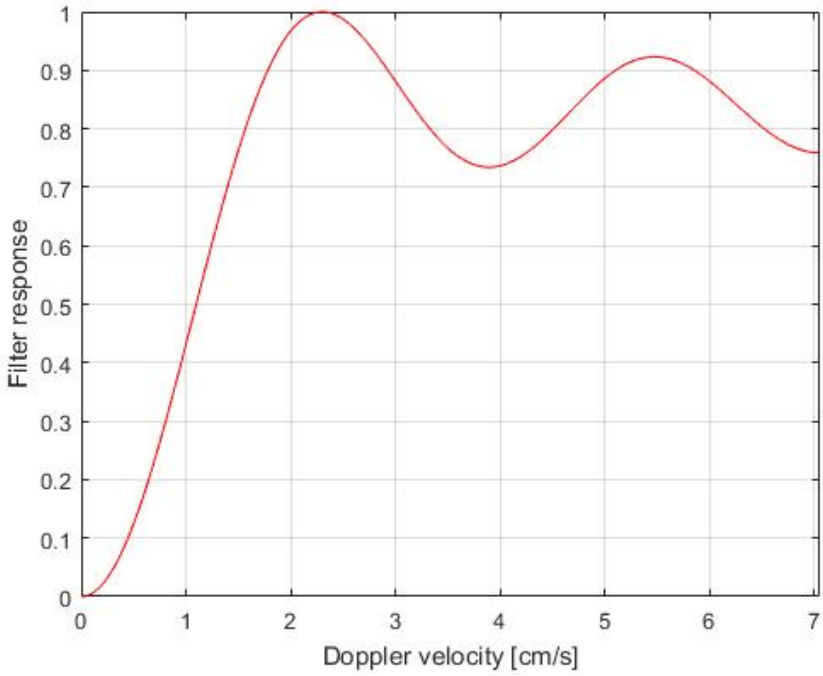

Figure 3.12: Filter response for the experiment with a PRF 10000 Hz.

The script used for the clutter filtering of the acquired signals was also written in MATLAB and has been attached as complementary material.

Chapter 4

Results

This chapter presents the results from the characterization of the PVA samples, the user interface programmed for the control of the robot, and the results from the experimental setup for coronary artery blood flow.

4.1 Characterization of PVA samples

The influence of the F-T cycles on the mechanical properties of PVA cryogel was investigated. Two sets of samples were fabricated, one using F-T 12 hour cycles, and the other using F-T 24 hour cycles.
Each set consisted of two PVA samples that allowed us to have a rough estimate of the reproducibility of the mechanical properties. Each estimate was measured at least 5 times to reduce the measurement uncertainty.

The longitudinal, and shear wave velocity for all PVA samples were calculated and plotted in MATLAB R2016b. The scripts used for the calculation of both longitudinal, and shear wave velocity can be found in Appendix D.

4.1.1 Longitudinal Velocity Results

Table 4.1 shows the longitudinal velocity measurement results from all PVA samples with both 12h, and 24h F-T cycle duration:

F-T duration	12h		24h	
Number of cycles	Sample 1 [m/s]	Sample 2 [m/s]	Sample 1 [m/s]	Sample 2 [m/s]
2	1493.13	1495.25	1493.10	1493.00
3	1494.79	1494.66	1493.50	1493.60
4	1493.97	1494.81	1491.40	1491.20
5	1491.56	1491.33	1488.80	1491.20

Table 4.1: Longitudinal velocity measurement results in PVA samples with different F-T cycle duration.

Figure 4.1 shows that sound speed slightly decreases with the number of F-T cycles. Still the maximum variation (about 7 m/s) only means a 0.5% of the mean sound speed (1493 m/s). The difference between the 12h and the 24h cycles is minimal, amounting for 3.7 m/s.

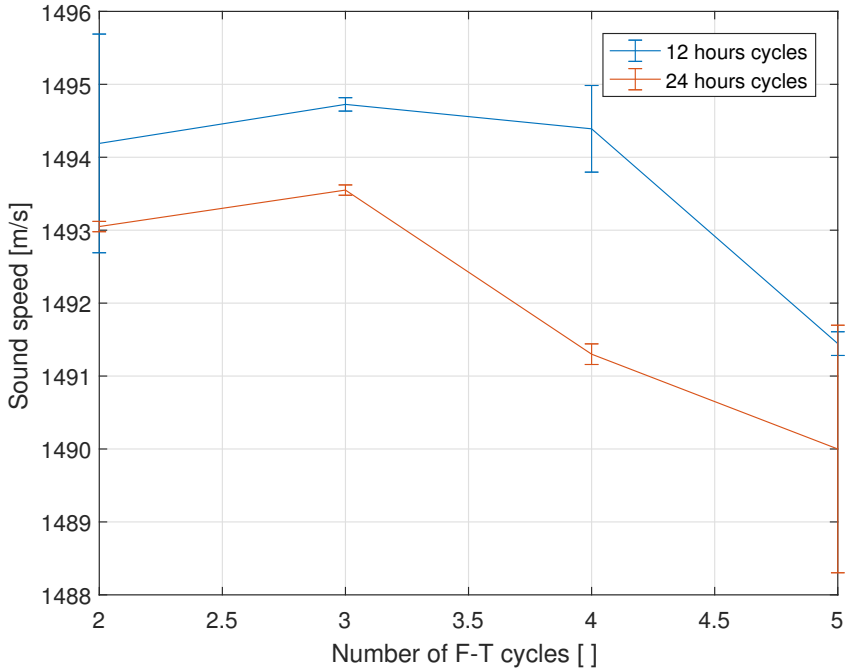

Figure 4.1: Mean longitudinal velocity in PVA samples subjected to a total of 5 F-T cycles with different duration.

As it can be seen in Figure 4.1, the mean longitudinal velocity for the PVA sample with 12h cycles is higher than for the sample with 24h at every cycle. However, the longitudinal velocity for the PVA samples decreases as the number of F-T cycles increases regardless

of the duration of the cycle. Despite the experimental variability, the sound speed is quite uniform, with less than 0.5% variation.

4.1.2 Shear Wave Velocity Results

Table 4.2 shows the shear wave velocity measurement results for the PVA samples with 12 and 24 hours cycle:

F-T duration	12h		24h	
Number of cycles	Sample 1 [m/s]	Sample 2 [m/s]	Sample 1 [m/s]	Sample 2 [m/s]
2	3.24 ± 0.24	3.11 ± 0.50	3.79 ± 0.49	3.91 ± 0.55
3	4.27 ± 0.44	4.45 ± 0.35	4.09 ± 0.51	4.24 ± 1.01
4	5.04 ± 0.56	5.57 ± 0.54	4.71 ± 0.86	4.85 ± 0.58
5	5.44 ± 1.37	5.85 ± 0.58	5.35 ± 0.63	5.12 ± 0.59

Table 4.2: Shear wave velocity measurement results in PVA samples with different F-T cycle duration.

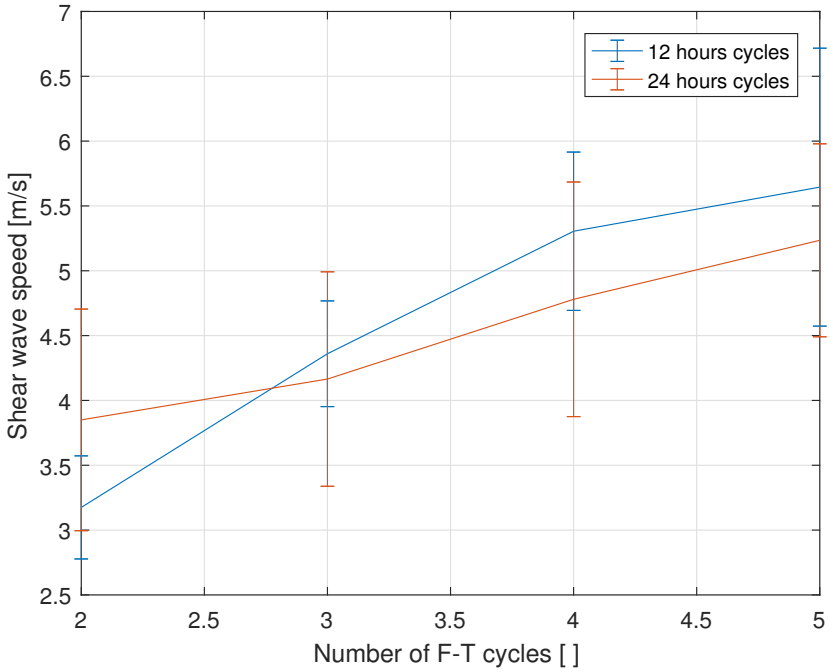

Figure 4.2: Mean Shear Wave Velocity in PVA samples after multiple F-T cycles with different cycle duration.

From Figure 2.11 we see that, as expected, the shear wave velocity increases with the number of F-T cycles. We observe a mean increase of 0.82 m/s/cycle using 12h cycles, and of 0.46 m/s/cycle using 24h cycles. However, the experimental uncertainty is high: 13.1% for the 12h cycle samples, and 18.8% for the 24h cycle samples. This not allow us to state that the shear wave velocity increase of the 12h is larger than that of the 24h cycles. The difference is most probably due to experimental variability.

Figure 4.3 shows the TDI velocity maps for SWV. These velocity maps show how the shear waves propagate through the PVA sample over time. The shear waves propagate from the focal point (the middle) and toward the edges. The slope of the propagating wavefront that gives shear wave velocity. The steeper the slope, the higher the shear wave velocity in the sample.

Overall, it can be seen that the slopes are steeper as the F-T cycles increases. This is common for both 12h and 24h samples as Figures 4.3 shows. In other words, the rate of change in the lateral position with respect to time is higher as the F-T cycles increases given a higher shear wave velocity.

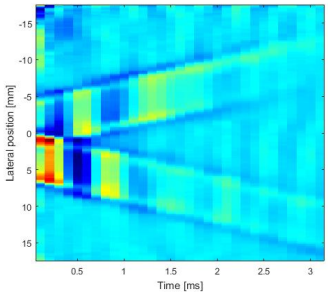

(a) 2 F-T cycles with 12h duration

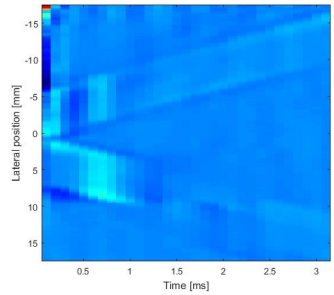

(b) 2 F-T cycles with 24h duration

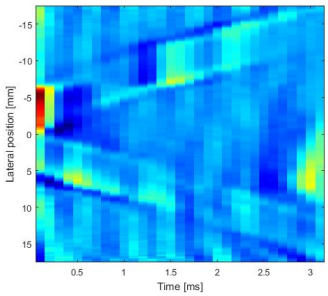

(c) 3 F-T cycles with 12h duration

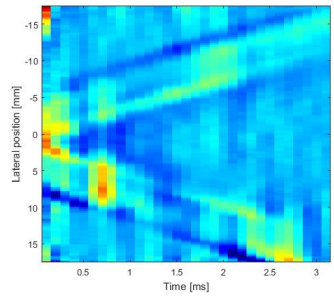

(d) 3 F-T cycles with 24h duration

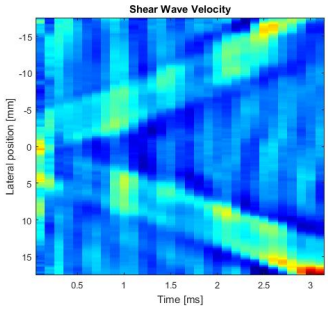

(e) 4 F-T cycles with 12h duration

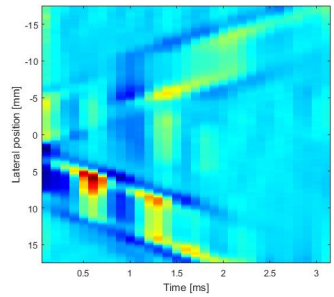

(f) 4 F-T cycles with 24h duration

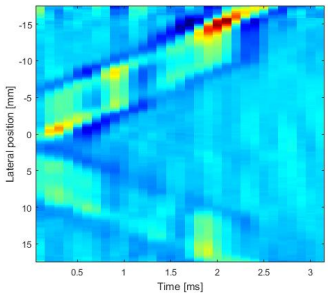

(g) 5 F-T cycles with 12h duration

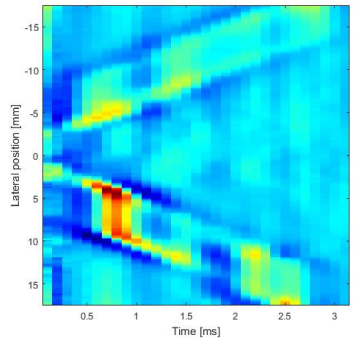

(h) 5 F-T cycles with 24h duration

Figure 4.3: TDI maps in PVA samples with different F-T duration and number of cycles.

4.2 User Interface

Figure 4.4 shows the final result of the graphic user interface (GUI) programmed in MATLAB. MATLAB apps are self-contained MATLAB programs with GUI front ends that automate a task or calculation. The GUI typically contains controls such as menus, toolbars, buttons, and sliders.
The robot control GUI was created to satisfy the user requirements stated in Section 3.4.2 and to facilitate the task of controlling the robot.

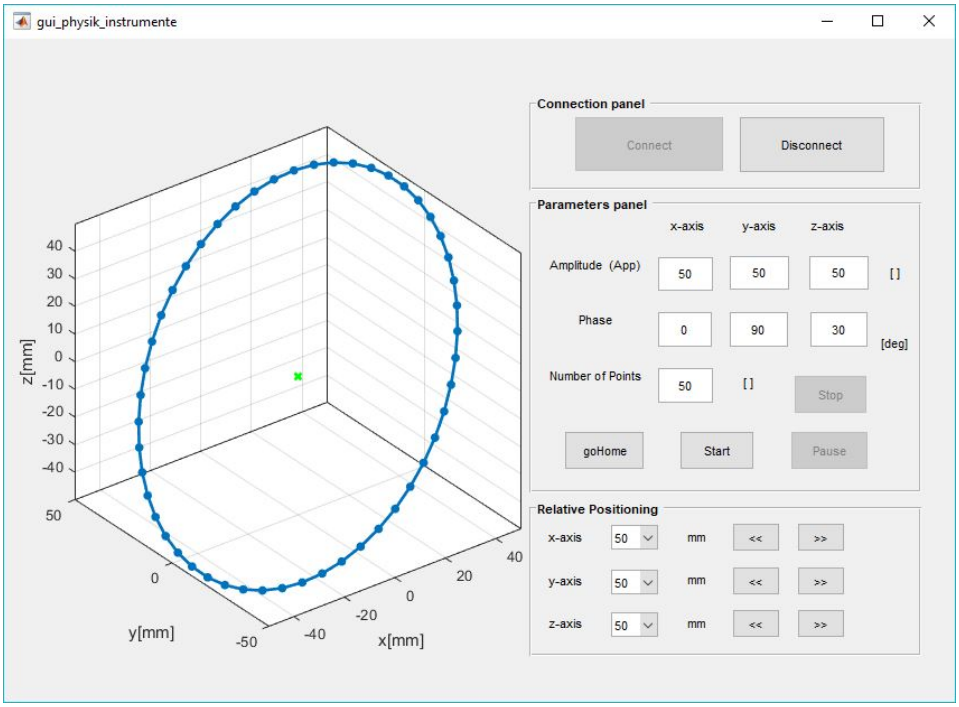

Figure 4.4: Graphical User Interface for Robot Control

As it can be seen in Figure 4.4, there was implemented three control panels. The connection panel contains two buttons which allow the user to connect and disconnect from the robot when pushed.
The parameters panel contain different elements related to the signal simulation and trajectory control. There are 7 text fields to edit the parameters as stated in Equation (2.16) which are used to simulate the periodic signal as Equation (2.15). The parameters can be edited while the robot is connected and not moving.

The total robot trajectory is calculated using Equation (2.17) and displayed in a 3D plot. The current robot position is also displayed and updated if there are any changes in the parameters field and as the robot position changes. The start push button starts the simulation when pushed, and it can be paused by pushing the pause button which causes

the robot to stop and resume at the same position. The simulation can also be completely stopped by pushing the stop button which redirects the robot to the initial position.

The goHome button moves the robot to the origin, which is favorable when modifying the software boundaries. With this, the origin is redefined as the initial position which gives an equal range of motion in the positive and negative axis direction.

The relative positioning panel allows the user to move the robot n steps in each axis direction relative to the current position. The steps are given in millimeter and are implemented as sliders with different step values. The positive and negative axes directions are implemented as push buttons with the arrows pointing to the right in the positive direction and to the left for the negative axis direction.

Most of the buttons are constrained with a disabling mechanism implemented to increase the performance. All buttons except the connect button are disabled when launching the program. The buttons are disabled after they are pushed once, and are enabled only if they are required to. For example, the connect button is disabled after it has been pushed once and remains that way since the robot is connected and there is no need to connect again. This also applies to the disconnect button.
The start button is, for instance, constrained by the input parameters. Several tests are run to check the validity of the parameters before calculating the robot trajectory and enabling the start button. One of these constraints is the number of points to be simulated, this must be higher than zero.

The stop and pause buttons are constrained by the start button and are only enabled after the simulation has started. The goHome button is only constrained by the motion robot status. As long as the robot is connected and not moving, the goHome is enabled and can be pushed.

The relative movement buttons are constrained by the range motion of the robot. If the relative movement step chosen is too high, or the robot has reached the maximum software boundary in one direction, then the corresponding button is disabled.

A video of a signal simulation using the robot, and with an amplitude in the z-axis of 2.5 mm and 100 points has been attached as a supplementary file.

4.3 Clutter Filtering Results

The acquired signals from the in-vitro experiments were loaded, and the parameters such as the scan and beam orientation defined. This signal was beamformed and filtered using a high-pass FIR filter with the parameters in Equation 3.1. The blood flow was visualized using Power Doppler (PD) images.

The code used for clutter filtering and the videos of the acquired signal before and after clutter filtering in each experiment are included as supplementary files.

This section presents all the results from clutter filtering the signal acquired in all experiments, and it is divided into two subsections. Section 4.3.1 presents the results of simulating tissue motion by pressurizing the ventricle cavity with a pulsatile water pump. Section 4.3.2 presents the results of simulating tissue motion by moving the probe with the robot. The results are presented in the same order as listed in Table 3.2 and 3.3.

4.3.1 Ventricle Motion Using the Pulsatile-pump System

No tissue motion, PRF=10000 Hz

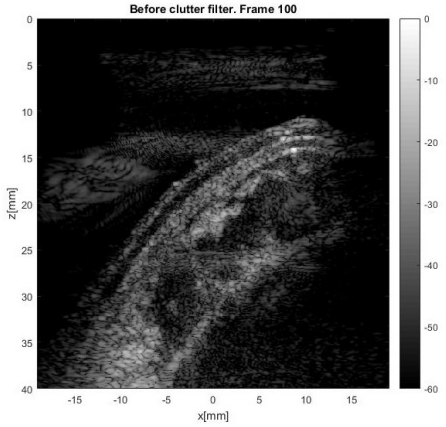

(a) Acquired signal before clutter filtering.

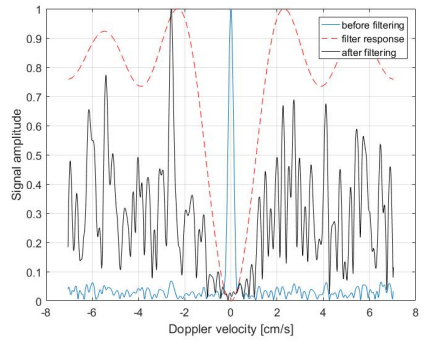

(b) Spectra of the filter, and signal before and after clutter filtering.

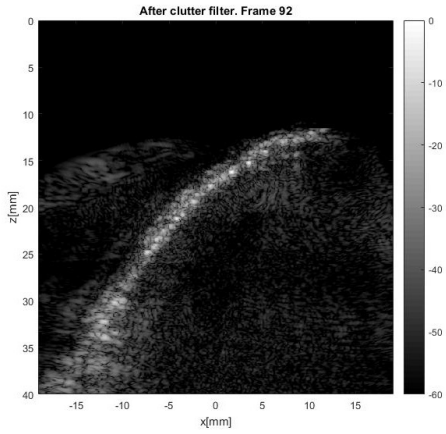

(c) Acquired signal after clutter filtering.

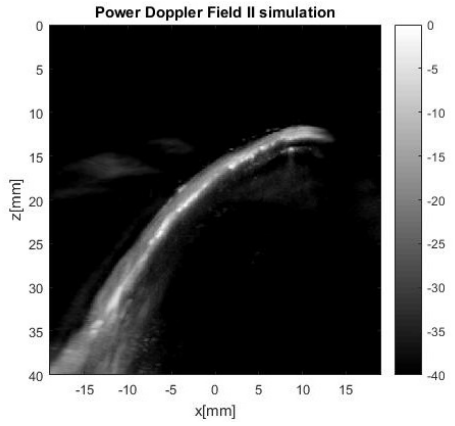

(d) Power Doppler visualization of the blood flow.

Figure 4.5: Clutter filtering of acquired signal using a PRF of 10000 Hz, and the ventricle at rest.

Figure 4.5 shows the results for the acquired signal with the ventricle at rest, and using a PRF of 10000 Hz. Due to the low scattering intensity of blood, the blood signal gets completely cluttered by the stationary signal from tissue.

As it can be seen in Figure 4.5a, the artery walls, and the ventricle structure can be visualized, while the blood can not. Figure 4.5b shows the spectra of the acquired signal before and after clutter filtering, and the filter response. We can see that the acquired signal contains a clutter component with a Doppler velocity around zero. The filter is able to remove completely this clutter component, leaving only the signals from blood. Figure 4.5c shows the beamformed signal after clutter filtering, where only the signal from blood is displayed. Figure 4.5d shows an image of the blood flow with the Power Doppler technique.

The results show that the FIR filter is able to remove the clutter component from the signal acquired with a PRF of 10000 Hz.

40 bpm tissue motion, PRF=10000 Hz

Figure 4.6 shows the clutter filtering results from the second experiment. Tissue motion was simulated using an amplitude of 40% in the flow pump, a pulse rate of 40 bpm; and the dataset was acquired using a PRF of 10000 Hz.

Figures 4.6a and 4.6c show the acquired signal before and after clutter filtering, respectively. Before cluttering filtering only tissue is visualized in the B-mode image. The spectra in Figure 4.6b show that the clutter component, still centered at v=0 m/s is completely removed after filtering. Only the blood signal is displayed in the filtered B-mode image in Figure 4.6c. The blood flow can be visualized by the power Doppler image in Figure 4.6d.

By comparing Figures 4.5d and 4.6d, it seems that the response from the filtered signal is similar. The results show a good performance of the clutter filter for this experiment as well.

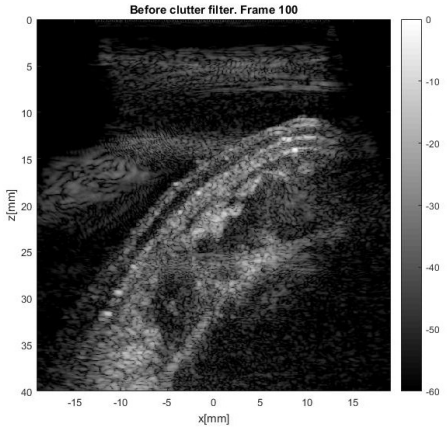

(a) Acquired signal before clutter filtering.

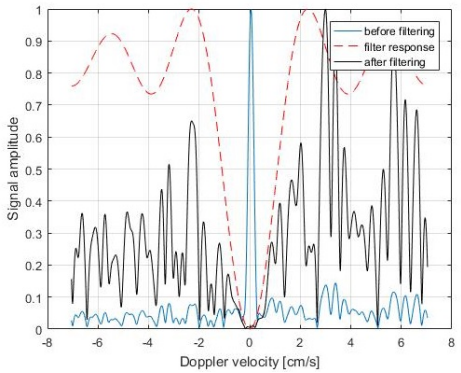

(b) Filter spectra and signal spectra from before, and after clutter filtering.

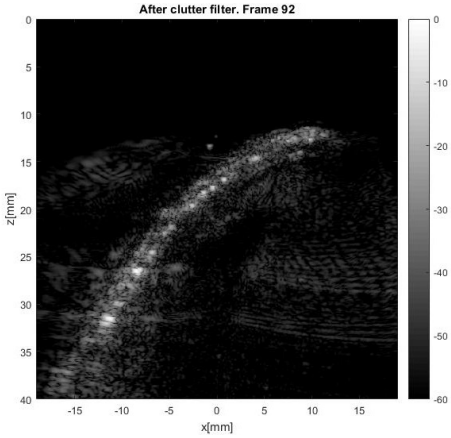

(c) Acquired signal after clutter filtering.

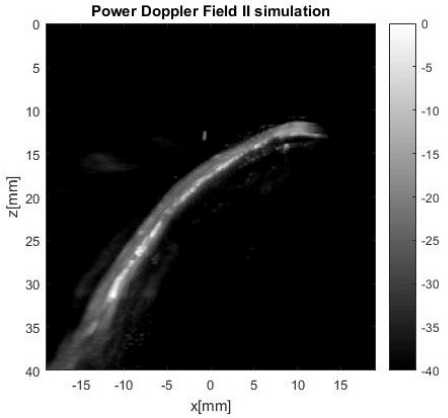

(d) Power Doppler visualization of the blood flow.

Figure 4.6: Clutter filtering of acquired signal using a PRF of 10000 Hz, and a tissue motion with an amplitude of 40% and pulse rate of 40 bpm.

70 bpm tissue motion, PRF=10000 Hz

Figure 4.7 shows results from the experiment using a PRF of 10000 Hz, an amplitude of 60%, and a pulse rate of 70 bpm for tissue motion.

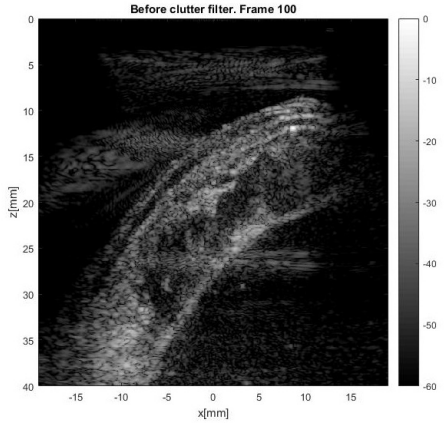

(a) Acquired signal before clutter filtering.

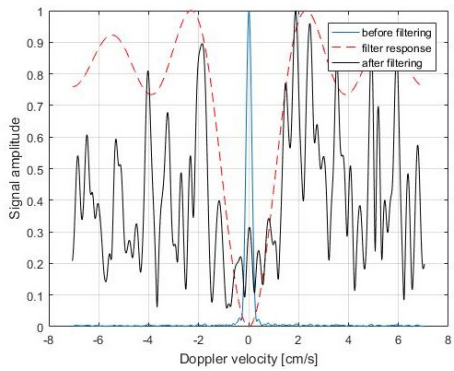

(b) Filter spectra and signal spectra from before, and after clutter filtering.

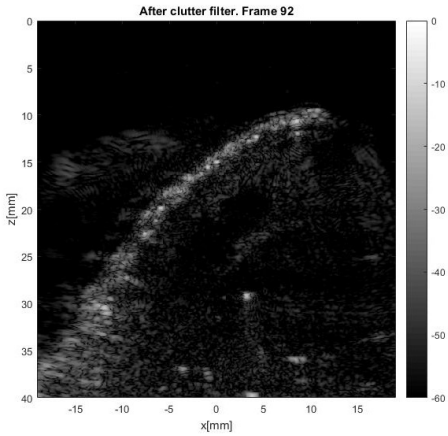

(c) Acquired signal after clutter filtering.

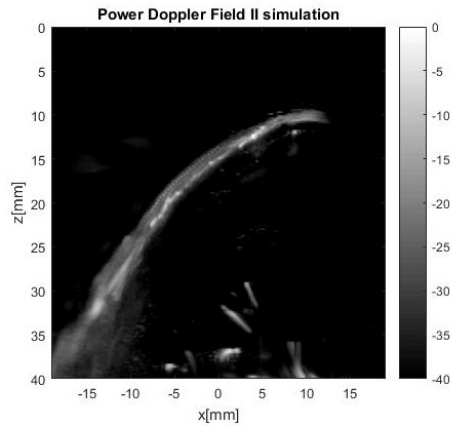

(d) Power Doppler visualization of the blood flow.

Figure 4.7: Clutter filtering of acquired signal using a PRF of 10000 Hz, and a tissue motion with an amplitude of 60% and pulse rate of 70 bpm

As it can be seen in Figure 4.7b, the acquired signal contains a strong clutter component with a high amplitude and a Doppler velocity around zero. This strong component corresponds to the tissue signal visible in Figure 4.7a. The spectra of the signal after clutter filtering shows that the filter is able to remove this clutter component resulting in a good imaging of the blood signals as seen in Figure 4.7c. We can see some tissue after filtering the signal, but the effect is small. Figure 4.7d shows a good PD image of the blood flow.

The results show that the filter performance decreases as the tissue motion increases. However, the performance of the filter at 10000 Hz is good in general and we do not see much clutter noise even for the highest tissue velocity (60%, 70 bpm).

No tissue motion, PRF=5000 Hz

Figure 4.8 shows the clutter filtering results for the experiment using a PRF of 5000 Hz for data acquisition.

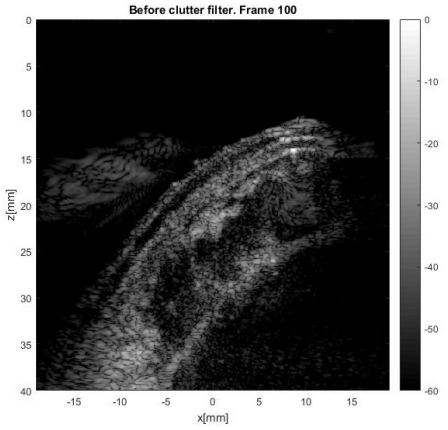

(a) Acquired signal before clutter filtering.

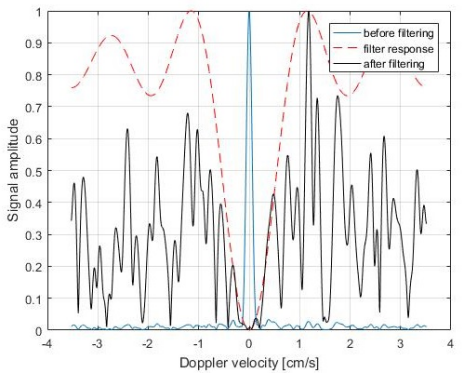

(b) Filter spectra and signal spectra from before, and after clutter filtering.

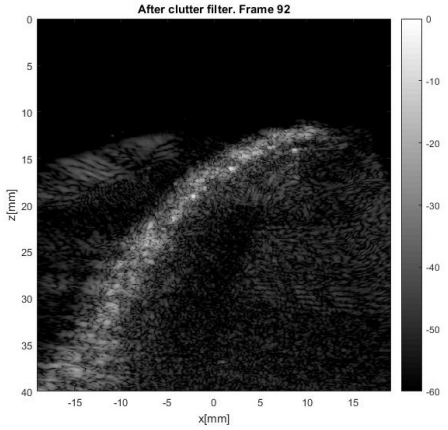

(c) Acquired signal after clutter filtering.

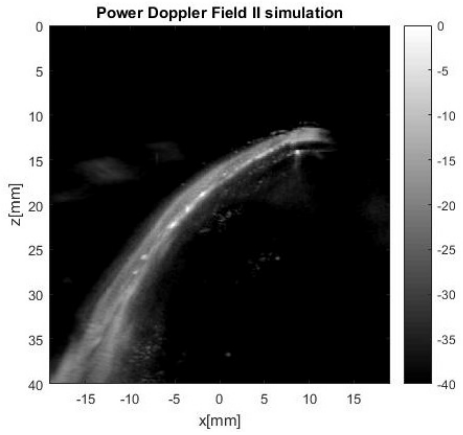

(d) Power Doppler visualization of the blood flow.

Figure 4.8: Clutter filtering of acquired signal using a PRF of 5000 Hz, and the ventricle at rest.

The blood signal can not be observed in Figure 4.8a. The filter response, and the signal spectra before and after clutter filtering can be seen in Figure 4.8b. As for the previous experiments using a PRF of 10000 Hz, we can see that the clutter component from the signal before filtering contains a strong clutter component. The component is completely removed after filtering. Figures 4.8c and 4.8b shows a good visualization of the fluid and flow.

40 bpm tissue motion, PRF=5000 Hz

Figure 4.9 shows the clutter filtering results from the second experiment using a PRF of 5000 Hz, and in which tissue motion was generated using an amplitude of 40% in the water pump, and a pulse rate of 40 bpm.

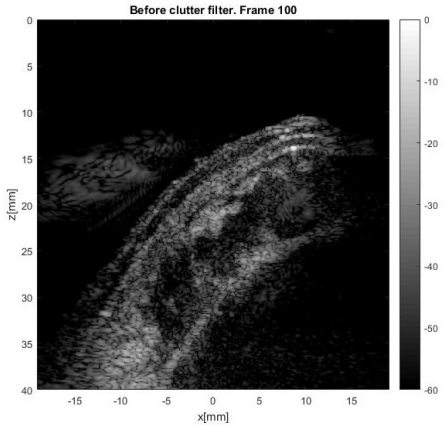

(a) Acquired signal before clutter filtering.

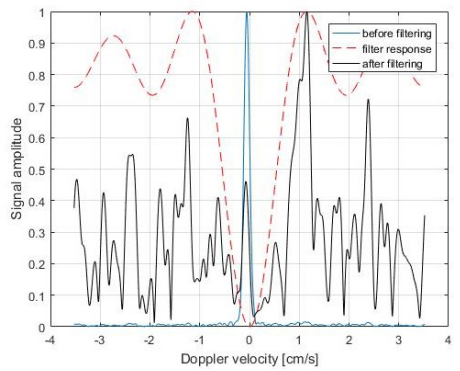

(b) Filter spectra and signal spectra from before, and after clutter filtering.

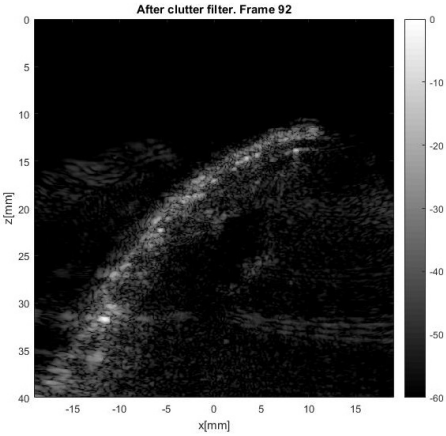

(c) Acquired signal after clutter filtering.

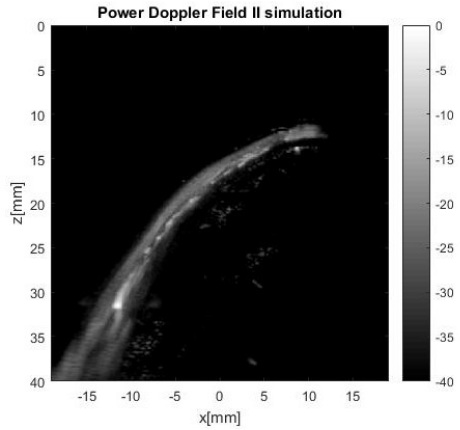

(d) Power Doppler visualization of the blood flow.

Figure 4.9: Clutter filtering of acquired signal using a PRF of 5000 Hz, and a tissue motion with an amplitude of 40% and pulse rate of 40 bpm.

Figures 4.9a and 4.9c, shows the acquired signal before and after clutter filtering. The clutter component from the tissue motion before clutter filtering can be seen in Figure 4.9b. By studying signal response before clutter filtering, we see that the clutter component is not centered at zero. However, the Doppler velocity shift of the tissue signal is small.

The blood signal and tissue signal are still separable, and most of the clutter component is stopped by the filter.

Figures 4.9c and 4.9d show a good image of the blood flow after clutter filtering. The performance of the filter is good for a PRF value of 5000 Hz and tissue motion of 40 bpm.

70 bpm tissue motion, PRF=5000 Hz

Figure 4.10 shows the results from the experiment with a tissue motion of 70 bpm, and 60% amplitude.

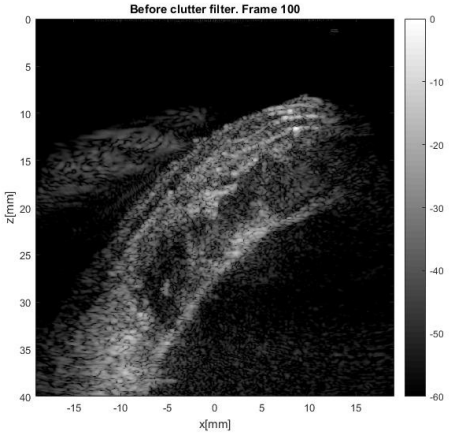

(a) Acquired signal before clutter filtering.

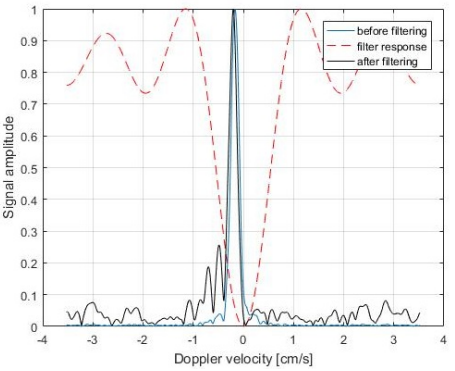

(b) Filter spectra and signal spectra from before, and after clutter filtering.

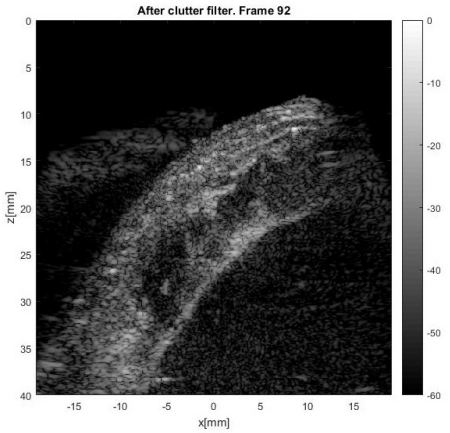

(c) Acquired signal after clutter filtering.

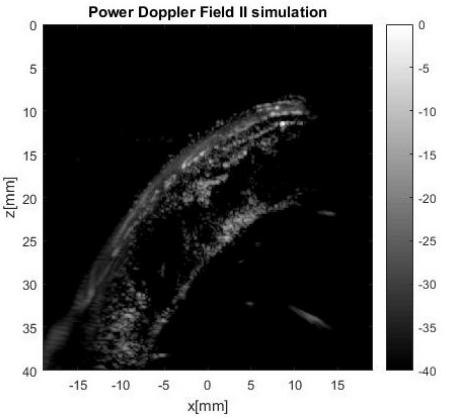

(d) Power Doppler visualization of the blood flow.

Figure 4.10: Clutter filtering of acquired signal using a PRF of 5000 Hz, and a tissue motion with an amplitude of 60% and pulse rate of 70 bpm.

Tissue signal is stronger than the blood signal, as we can see both on Figure 4.10a and Figure 4.10c. The filter response and signal response before and after clutter filtering is shown in Figure 4.10b. For a tissue motion of 70 bpm, we see that the Doppler velocity has been shifted to -0.17 cm/s. The filter performance has decreased letting some clutter components pass through. This results in the display of both clutter and blood signal as shown in Figure 4.10c. The Power Doppler (Figure 4.10d) shows the blood flow, but we can also see the ventricle structure.

No tissue motion, PRF=2000 Hz

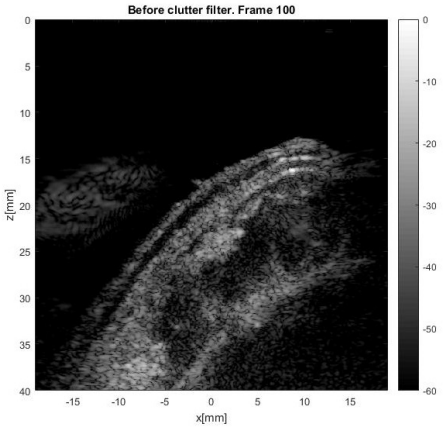

(a) Acquired signal before clutter filtering.

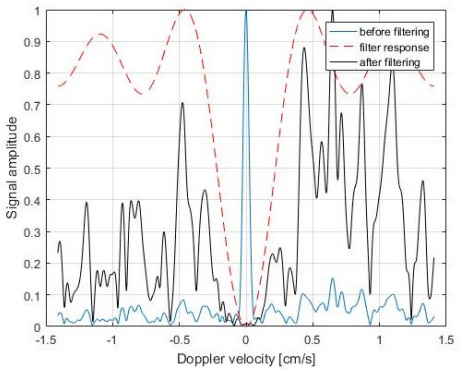

(b) Filter spectra and signal spectra from before, and after clutter filtering.

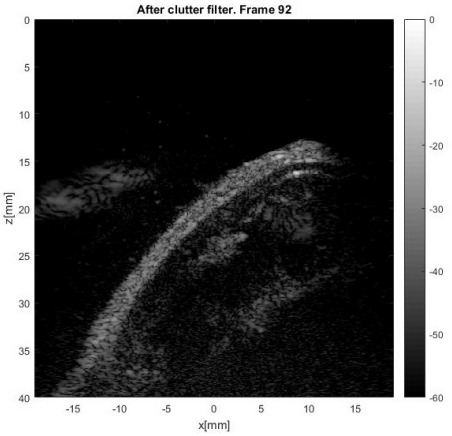

(c) Acquired signal after clutter filtering.

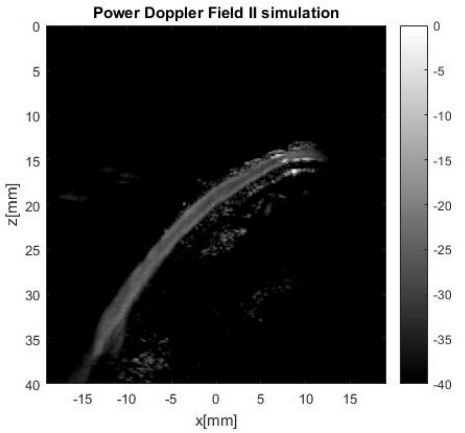

(d) Power Doppler visualization of the blood flow.

Figure 4.11: Clutter filtering of acquired signal using a PRF of 2000 Hz, and with the ventricle at rest.

Figure 4.11 shows the clutter filtering results of the signal acquired using a PRF of 2000 Hz, and with the ventricle at rest.

Figure 4.11a shows an image in which the blood flow through the coronary can not be visualized because is obscured by the signals coming from the tissue. The signal response before clutter filtering shows that the Doppler velocity of the clutter component from the acquired signal is centered at zero. The filter response in Figure 4.11b shows that this clutter component is removed by the filter, and thus the tissue signal is completely removed. After filtering, only the blood spectrum remains, giving a good image of the blood flow as shown in Figure 4.11c and Figure 4.11d.

40 bpm tissue motion, PRF=2000 Hz

For the experiment, a PRF of 2000 Hz was used and tissue motion of 40 bpm and an amplitude of 40%. The results are shown in Figure 4.12.

As it can be in Figures 4.12a and 4.13c, the signal after clutter filtering is almost the same as before filtering. The spectra of the signal before clutter filtering, in 4.12b, shows that the signals from blood and clutter are not separable. We see that the Doppler velocity for the clutter component has shifted in the positive direction, and covers the band from 0 to almost 0.5 cm/s. Due to this, the filter is not able to remove the clutter components. The filter performance for the acquired signal using a PRF of 2000 Hz is therefore poor, and the tissue is visualized both in Figure 4.12c and Figure 4.12d.

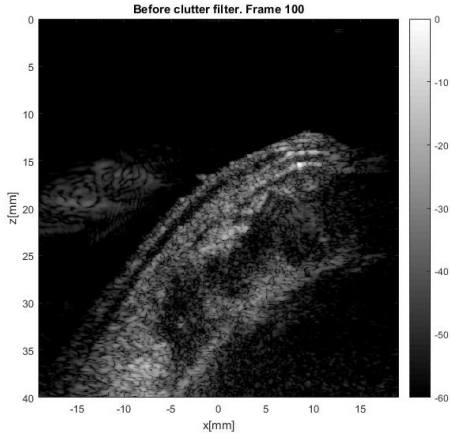

(a) Acquired signal before clutter filtering.

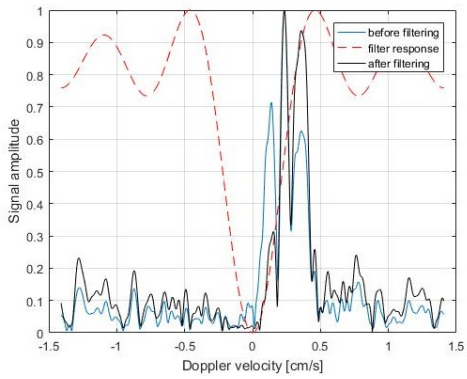

(b) Filter spectra and signal spectra from before, and after clutter filtering.

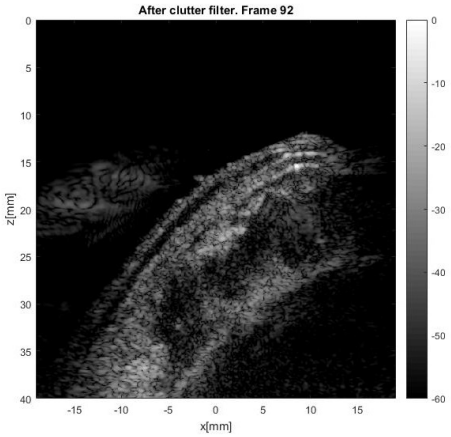

(c) Acquired signal after clutter filtering.

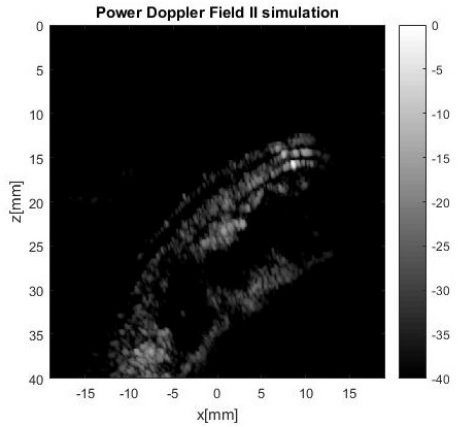

(d) Power Doppler visualization of the blood flow.

Figure 4.12: Clutter filtering of acquired signal using a PRF of 2000 Hz, and a tissue motion with an amplitude of 40% and pulse rate of 40 bpm.

70 bpm tissue motion, PRF=2000 Hz

For this experiment the tissue motion was generated with a pulse of 70 bpm and an amplitude of 60%, and a PRF of 2000 Hz.
As it can be seen in Figure 4.13c, the beamformed image contains tissue signal. The filter performance for this experiment is worse than from all the previous experiments. After clutter filtering (Figure 4.13c), the blood flow is not visualized, which is as expected due to the so high tissue movement which makes it difficult to separate the blood and clutter signals.

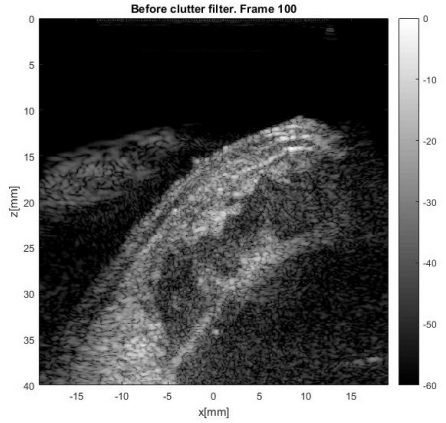

(a) Acquired signal before clutter filtering.

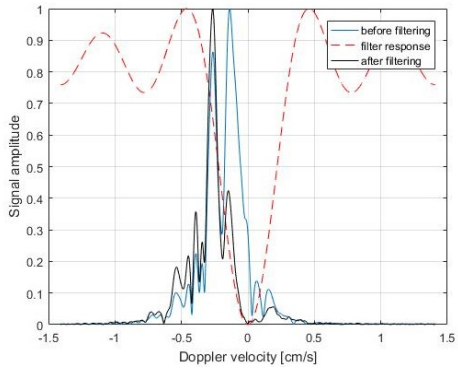

(b) Filter spectra and signal spectra from before, and after clutter filtering.

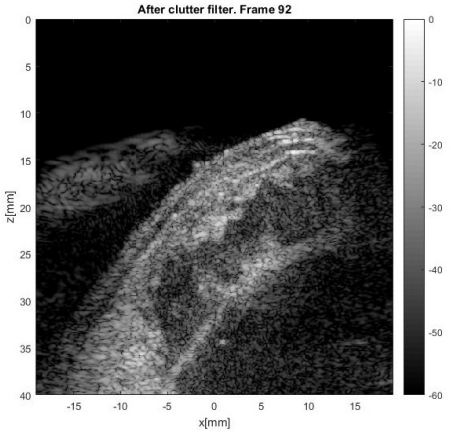

(c) Acquired signal after clutter filtering.

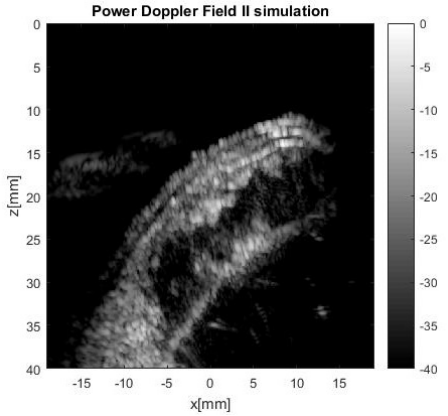

(d) Power Doppler visualization of the blood flow.

Figure 4.13: Clutter filtering of acquired signal using a PRF of 2000 Hz, and a tissue motion with an amplitude of 60% and pulse rate of 70 bpm.

The spectra of the signal before clutter filtering shows that the signal contains clutter components with Doppler velocities that covers the band from -0.6 to almost 0.2 cm/s. The filter response as shown 4.13b, shows that the filter fails to remove clutter signals. After applying the filter, the blood flow can not be visualized as tissue signal is strong (4.13d). The relative movement is so high in this case, that it is shown in the PD image as a blurred contour of the tissue structures.

4.3.2 Tissue Motion Using the Robot

Tissue motion with 0.5 mm amplitude

The results of this experiment using the robot are shown in Figure 4.14. The ventricle movement was generated with an amplitude of 0.5 mm in the z-axis, and 100 points.

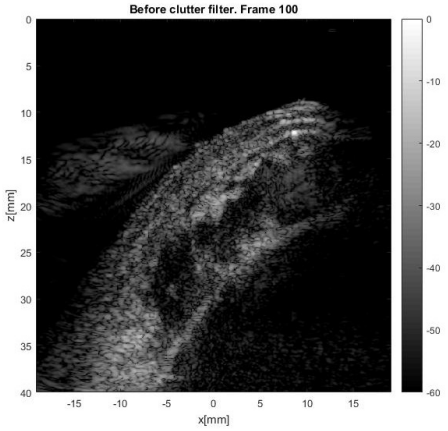

(a) Acquired signal before clutter filtering.

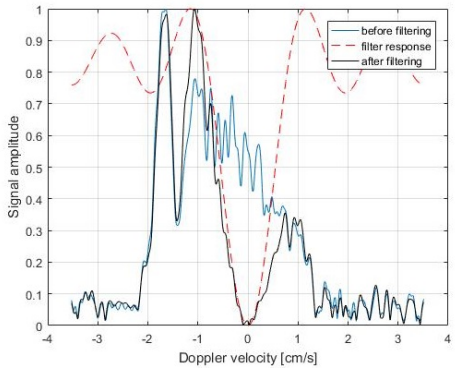

(b) Filter spectra and signal spectra from before, and after clutter filtering.

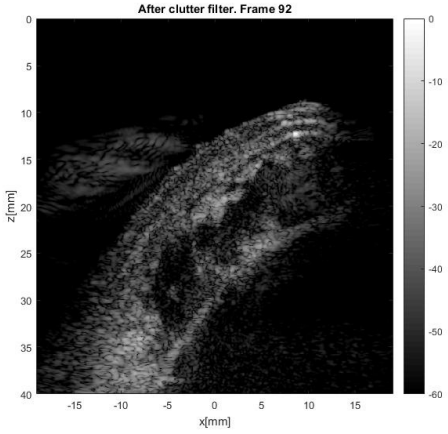

(c) Acquired signal after clutter filtering.

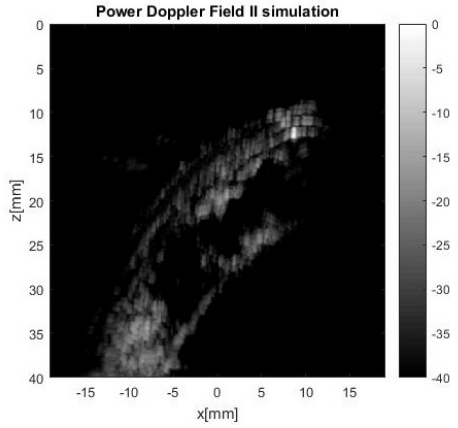

(d) Power Doppler visualization of the blood flow.

Figure 4.14: Clutter filtering of acquired signal using the robot, and a tissue motion with an amplitude of 0.5 mm and 100 points.

The filter response as in Figure 4.14b shows that the filter fails to remove the clutter signals as they cover the band from -2.2 to 1.3 cm/s. After applying the filter, the tissue signal is not eliminated and thus it is displayed in Figure 4.14c.

By comparing the images of the signal before and after clutter filtering, it is difficult to see any improvement in the visualization of the blood flow. As before, the tissue motion is high that we can see in Figure 4.14d, the Power Doppler image is smeared out.

Tissue motion with 1.5 mm amplitude

For the second tissue motion simulation using the robot, the displacement amplitude was increased to 1.5 mm. The number of points was the same as before: 100. The results of this experiment are shown in Figure 4.15.

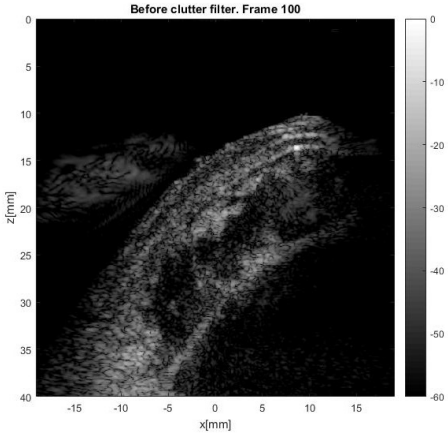

(a) Acquired signal before clutter filtering.

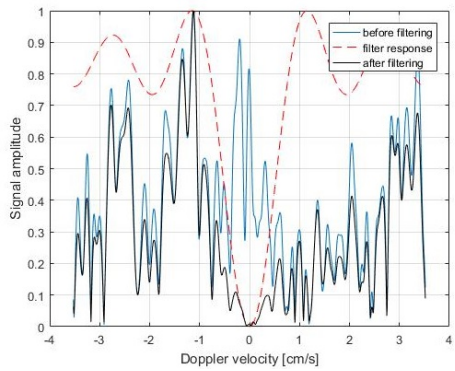

(b) Filter spectra and signal spectra from before, and after clutter filtering.

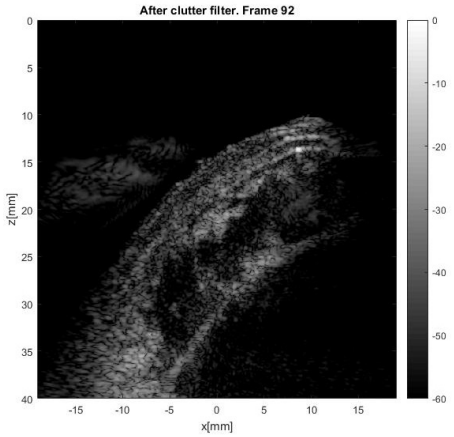

(c) Acquired signal after clutter filtering.

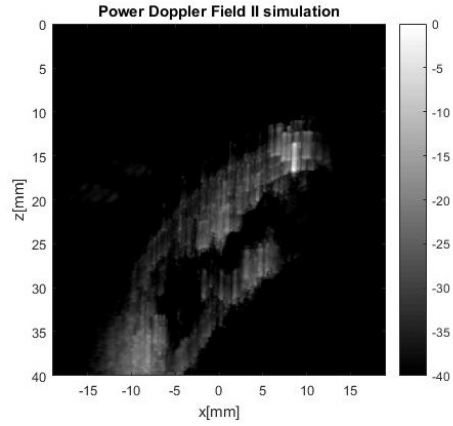

(d) Power Doppler visualization of the blood flow.

Figure 4.15: Clutter filtering of acquired signal using the robot, and a tissue motion with an amplitude of 1.5 mm and 100 points.

Figures 4.15a and 4.15c shows the signal before and after clutter filtering, respectively. The signal response before clutter filtering shows that the clutter velocities dominate over the signals from blood, and are therefore not easily separable. The filter response in Figure 4.15b shows that the performance of the filter is very poor, and thus it fails to separate the signals. This results in a poor visualization of the blood flow in Power Doppler imaging as shown in Figure 4.15d. By comparing the images before and after clutter filtering, we see no improvement.

Tissue motion with 2.5 mm amplitude

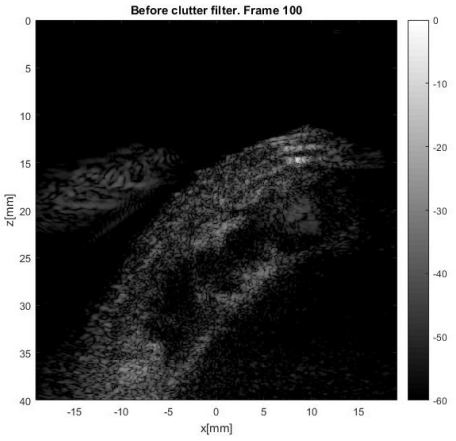

(a) Acquired signal before clutter filtering.

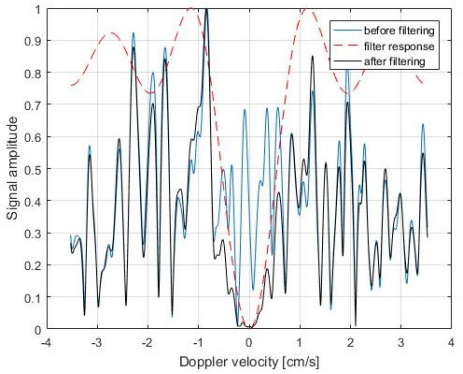

(b) Filter spectra and signal spectra from before, and after clutter filtering.

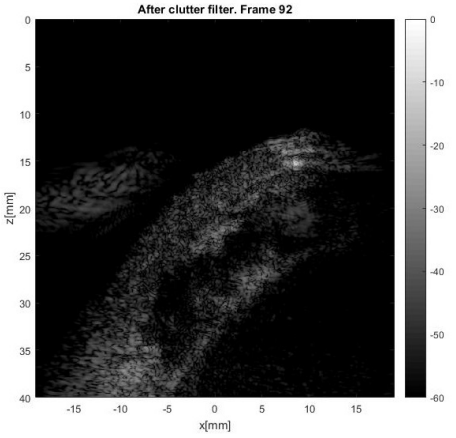

(c) Acquired signal after clutter filtering.

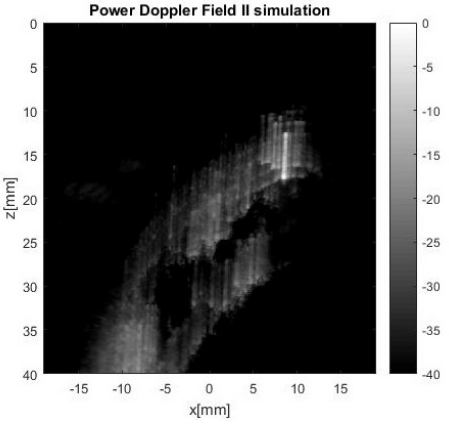

(d) Power Doppler visualization of the blood flow.

Figure 4.16: Clutter filtering of acquired signal using the robot, and a tissue motion with an amplitude of 2.5 mm and 100 points.

The results of the last tissue motion controlled by the robot, with an amplitude of 2.5 mm, and 100 points are shown in Figure 4.16. Increasing the amplitude of the displacement means higher tissue velocity, and thus stronger clutter components.

Figure 4.16a shows the acquired signal before clutter filtering. The filter response in Figure 4.16b shows that it is impossible to distinguish between clutter and velocity components, which means that the clutter component is suffering also from aliasing. We can not see any improvement in the image of the filtered signal (4.16c). The clutter signals from tissue are so strong that they dominate over the blood signal. The Power Doppler image in Figure 4.16d shows a very poor visualization and completely smeared out.

The results show that the FIR filter fails to remove the signals acquired from the tissue motion using the robot in all three experiments.

Chapter 5

Discussion and Conclusion

The results from the characterization of the PVA samples in Section 4.1 show that the speed of sound in the PVA samples is uniform. The maximum variation of 7 m/s, which is 0.5% of the mean sound speed of 1490 m/s, is almost nonexistent.

The results of the shear wave velocity measurement show, as expected, that the mean shear wave velocity for the PVA samples increases with increasing the number of F-T cycles. The mean shear wave velocity for the 12h sample increases 0.82 m/s/cycle, while the increment is 0.46 m/s/cycle for the 24h sample. The high experimental uncertainty in the SWV measurement results does not allow us to conclude anything about the relation of the SWV between the samples with 12h and 24h cycle. Such a high experimental uncertainty may be due to measurement error, such as the manual measurement of the SWV using the TDI velocity maps to create a line parallel to the direction of the wavefront propagation. Another reason could be the inhomogeneity in the PVA samples causing the shear waves to propagate differently than in homogeneous tissue, resulting in an inaccurate velocity estimation.

While no big difference was observed between 12h and 24h cycles, it is recommended to increase the number of samples to reduce the experimental variability and check whether there is any difference in the increase of the shear wave velocity after each F-T cycle.

The robot was able to simulate the movement of the coronary artery with a periodic signal as described in Section 2.6. Although there were challenges in displaying the robot position for very low signal amplitudes, the robot was able to calculate and move to every point in the trajectory. It could also be seen that the robot movements were smoother as the number of points was higher, but the velocity at which the linear stages moved was affected. The robot was able to complete the desired trajectory and simulate the signal even at a lower speed. From the clutter filtering results, we observe, that a smaller step should be used to simulate lower tissue velocities. Due to time constraints, that measurement was not included in this report, but the experimental rig should be able to achieve even smaller

steps as it bestows an incremental resolution of 0.1 μm. Smaller displacements may provide a more realistic tissue motion as the one simulated with the pulsatile flow pump.

The pump controlled motion setup showed that a standard clutter filter worked fine for a PRF of 10000 Hz and 5000 Hz. For the 2000 Hz PRF case, tissue signal remained unfiltered using a 40 bpm and 70 bpm motion. A PRF of 2000 Hz, for a 7 plane-wave sequence, is rather low. This indicates that the motion must be increased in order to have a more realistic simulation of ventricular motion. However, to achieve that, the pump must be upgraded to produce a larger flow gradient. With the current setup, increasing the pulse frequency leads to a reduction of the amplitude of the ventricular displacement.

Alternatively, the PRF can be artificially reduced to increase the apparent tissue velocity, as done here, but then the coronary flow must also be scaled accordingly. Otherwise, the flow signal will be aliased.

Given the impossibility of increasing the amplitude of the ventricle's displacement we opted for reducing the PRF, and hence the aliased blood spectra showed in the Section 4.3. This aliasing makes invalid any velocity estimation with conventional Doppler techniques. The results can still be used, however, to produce Power Doppler images or velocity estimates with speckle tracking. We also observed that the scattering intensity of the fluid, a suspension of deionized water and Orgasol powder, was higher than that of blood. This may produce unrealistic results with too high signal-to-noise ratios.

Another method that could be used to know the ground truth of the coronary blood flow is 3D - Scanning Laser Vibrometry. This method uses light as a sensor and the Doppler effect for non-contact optical vibration measurement, eliminating the influence of a traditional contact transducer on the test object motion. This method includes spatial nature of the motion and helps to unravel the complex system dynamics of a test object. The motion of a complete surface can be measured by the sequential placement of light on a grid of points using scanning mirrors, and three measurement heads can be used to sample each grid point in three separate directions, determining the vector motion of that point [35].

We have managed to completed all the task for this project and to build a setup to simulate ventricular motion to test advanced clutter filtering techniques. Hopefully, this will help in the detection of coronary artery disease and help reduce the incidence of myocardial infarction.

Bibliography

[1] Hans Torp Steinar Bjærum and Kjell Kristoffersen. Clutter filter design for ultrasound color flow imaging. *IEEE transactions on ultrasonics, ferroelectrics, and frequency control*, 49(2), 2002.

[2] Winnie Yu Brindles Lee Macon and Lauren Reed-Guy. What is acute myocardial infarction? `http://www.healthline.com/health/acute-myocardial-infarction#overview1`, December 2015. Accessed: 2017-05-29.

[3] WebMD. Coronary artery disease. `http://www.webmd.com/heart-disease/guide/heart-disease-coronary-artery-disease#1`, June 2016. Accessed: 2017-05-30.

[4] World Health Organization. Prevention of recurrences of myocardial infarction and stroke study. `http://www.who.int/cardiovascular_diseases/priorities/secondary_prevention/country/en/index1.html`, March 2017. Accessed: 2017-06-11.

[5] Lung National Heart and Blood Institute. What is atherosclerosis? `https://www.nhlbi.nih.gov/health/health-topics/topics/atherosclerosis/`, June 2016. Accessed: 2017-05-30.

[6] WebMD. Blood clots. `http://www.webmd.com/dvt/blood-clots#1`, June 2016. Accessed: 2017-06-06.

[7] Reed Group MDGuidelines. Myocardial infarction, acute. `http://www.mdguidelines.com/myocardial-infarction-acute`, 2012. Accessed: 2017-05-30.

[8] Thomas L. Szabo. *Diagnostic Ultrasound Imaging: Inside Out, 1st Edition*. Elsevier Academic Press, 2004.

[9] Floyd A. Firestone. The supersonic reflectoscope, an instrument for inspecting the interior of solid parts by means of sound waves. *Journal of the Acoustical Society of Americae*, 17(3):287–299, 1946.

[10] Kevin Martin Peter Hoskins and Abigail Thrush. *Diagnostic Ultrasound: Physics and Equipment*. Cambridge University Press, 2010.

[11] Linda Gillam Bernard Bulwer Scott D. Solomon, Justina Wu. Echocardiography: Pulsed-wave and continuous-wave doppler. https://thoracickey.com/echocardiography/, June 2016. Accessed: 2017-06-06.

[12] Cleveland Clinic. What is a vascular ultrasound? https://health.clevelandclinic.org/2012/03/what-is-a-vascular-ultrasound/, March 2012. Accessed: 2017-06-08.

[13] Shoaib Muhammad. Blood flow types. https://www.slideshare.net/fastkool/blood-flow-types, 2014.

[14] F Fernandes, M Alam, S Smith, and F Khaja. The role of transesophageal echocardiography in identifying anomalous coronary arteries. *Circulation*, 88(6):2532–2540, 1993.

[15] Lung National Heart and Blood Institute. Coronary angiography? https://www.nhlbi.nih.gov/health/health-topics/topics/ca, December 2016. Accessed: 2017-06-08.

[16] Alexander V. Vrublevsky Alla A. Boshchenko and Rostislav S. Karpov. Transthoracic echocardiography in the detection of chronic total coronary artery occlusion. *European Journal of Echocardiography*, 10:62–68, 2009.

[17] A. Anjaneyulu. Evaluation of coronary arteries by transthoracic echocardiography. *Journal of The Indian Academy of Echocardiography and Cardiovascular Imaging*, 1(1):27–31, 2017.

[18] MedChrome Sulav Shrestha. Coronary circulation anatomy. http://tube.medchrome.com/2011/04/coronary-circulation-anatomy.html, March 2011. Accessed: 2017-06-08.

[19] Music Journey. Basic properties of sound. https://musicjourneys.wordpress.com/2013/03/10/6/, 2017. Accessed: 2017-04-18.

[20] G. Montaldo, M. Tanter, J. Bercoff, N. Benech, and M. Fink. Coherent plane-wave compounding for very high frame rate ultrasonography and transient elastography. *IEEE Transactions on Ultrasonics, Ferroelectrics, and Frequency Control*, 56(3):489–506, March 2009.

[21] Jørgen Avdal. *Model-Based Evaluation of Blood Velocity Estimation Techniques*. PhD thesis, Faculty of Medicine, Department of Circulation and Medical Imaging, Norwegian University of Science and Technology, April 2015.

[22] H. Torp. Clutter rejection filters in color flow imaging: a theoretical approach. *IEEE Transactions on Ultrasonics, Ferroelectrics, and Frequency Control*, 44(2):417–424, March 1997.

[23] Mark Wilson. The physics of diagnostic ultrasound frcr physics lectures. FRCR Physics Lectures, 2015.

[24] Daniel W. Rickey and Aaron Fenster. A doppler ultrasound clutter phantom. *Ultrasound in Medicine and Biology*, 22(6):747 – 766, 1996.

[25] Emilia Gómez Gutiérrez. Introducción al filtrado digital. SÍNTESI I PROCESSAMENT DEL SO I, Depatamento de Sonolodia, Escola Superior de Musica de Catalunya, Noviembre 2009.

[26] Jørgen Arendt Jensen. Field: A program for simulating ultrasound systems. *Medical and Biological Engineering and Computing*, 34(1):351–353, 1996.

[27] Jørgen Arendt Jensen and Niels Bruun Svendsen. Calculation of pressure fields from arbitrarily shaped, apodized, and excited ultrasound transducers. *IEEE TRANSACTIONS ON ULTRASONICS. FERROELECTRICS. AND FREQUENCY CONTROL*, 39(2), March 199.

[28] Kenneth C. Chu and Brian K. Rutt. Polyvinyl alcohol cryogel: An ideal phantom material for mr studies of arterial flow and elasticity. *Magnetic Resonance in Medicine*, 37(2):314–319, 1997.

[29] Christie M. Hassan and Nikolaos A. Peppas. *Structure and Applications of Poly(vinyl alcohol) Hydrogels Produced by Conventional Crosslinking or by Freezing/Thawing Methods*. Springer Berlin Heidelberg, Berlin, Heidelberg, 2000.

[30] Junru Wu. Determination of velocity and attenuation of shear waves using ultrasonic spectroscopy. *The Journal of the Acoustical Society of America*, 99(5):2871–2875, 1996.

[31] Benjamin Strandli Fermann. Assessment of supersonic shear imaging and pulse inversion techniques in shear wave elastography. TTT4510 SPECIALIZATION PROJECT, Faculty of Information Technology, Mathematics and Electrical Engineering, Norwegian University of Science and Technology, December 2016.

[32] Inc. Anaheim Automation. Linear actuator guide. `http://www.anaheimautomation.com/manuals/forms/linear-actuator-guide.php#sthash.dLxoWbWk.goEbguJC.dpbs`, 2017. Accessed: 2017-06-14.

[33] Eksma Optics. Motorized translation stage 960-0065. `http://eksmaoptics.com/opto-mechanical-components/motorized-positioners-and-controllers-900/motorized-translation-stage-960-0065/`. Accessed: 2017-06-17.

[34] Alyssa Ninoska Garcia Mayuri. Acoustic manipulation of cells in microfluidic devices. TKT 4550 - SPECIALIZATION PROJECT, Faculty of Information Technology, Mathematics and Electrical Engineering, Norwegian University of Science and Technology, December 2016.

[35] Polytec. Scanning vibrometers. http://www.polytec.com/us/products/vibration-sensors/scanning-vibrometers/. Accessed: 2017-06-20.

Appendix

Appendix A

List of supplementary files

1. Robot Code
    - Complete code for robot control user interface
2. Robot Documentation
    - Mercury Native Commands for C-863 DC- Motor Controller
3. Clutter Filtering
    - Clutter filtering code
    - Videos for tissue motion using the robot
    - Videos for tissue motion with of PRF 10000 Hz
    - Videos for tissue motion with of PRF 5000 Hz
    - Videos for tissue motion with of PRF 20000 Hz
4. Blood Flow Imaging
    - Code use for data acquisition using compound plane-wave imaging

Appendix B

Equipment list

B.1 Fabrication of PVA phantoms

- P1763 - Poly(vinyl alcohol) Fully hydrolyzed, Sigma-Aldrich
- Omega HH147 RS- 232 Data Logger Thermometer
- Grant OLS200 Orbital Shaking Water Bath
- Heidolph MR Hei-Standard magnetic stirrer
- Degassed and deionized water
- 500 mL Beaker glass
- Molds for all phantoms
- Magnetic stir bars
- Plastic teaspoon
- Plastic gloves
- 5 mL syringe
- 1 mL syringe
- Wipers

B.2 Characterization of PVA block samples

- Agilent $33522A$, 30 MHz Function / Arbitrary Waveform Generator
- Verasonics Vantage 256 Ultrasound Research system
- LeCroy WaveSurfer 42Xs-A, 400 MHz Oscilloscope
- Immersion transducers, C309-SU, 5 MHz (x2)
- PVA samples to be measured (x4)
- Degassed and deionized water
- L11 $-$ 4v linear array probe
- Quadratic Sample Holder
- BNC connector cables
- Water tank
- Clamps

B.3 Final experimental setup

- High-Precision Linear Translation Stage Motors by Physik Instrumente: M-521(5IM),M-521(5IS), M-531(5IM)
- Pulsed flow water pump with pressure regulator chamber
- Heart ventricle with coronary artery phantoms
- Rectangular water tank with ventricle holder
- Heidolph MR Hei-Standard magnetic stirrer
- Verasonics Vantage 256 research system
- L12 − 3v Linear array ultrasound probe
- Orgasol powder Type 3502 D NAT 1
- Continuous flow micro water pump
- Degassed and deionized water
- 500 mL Beaker glass
- 10 mm, Pastic tubes
- 5 mm, Plastic tubes
- Arduino Mega 2560
- Magnetic stir bar
- BNC cables
- Clamps

Appendix C

Robot control: Sequence Diagram

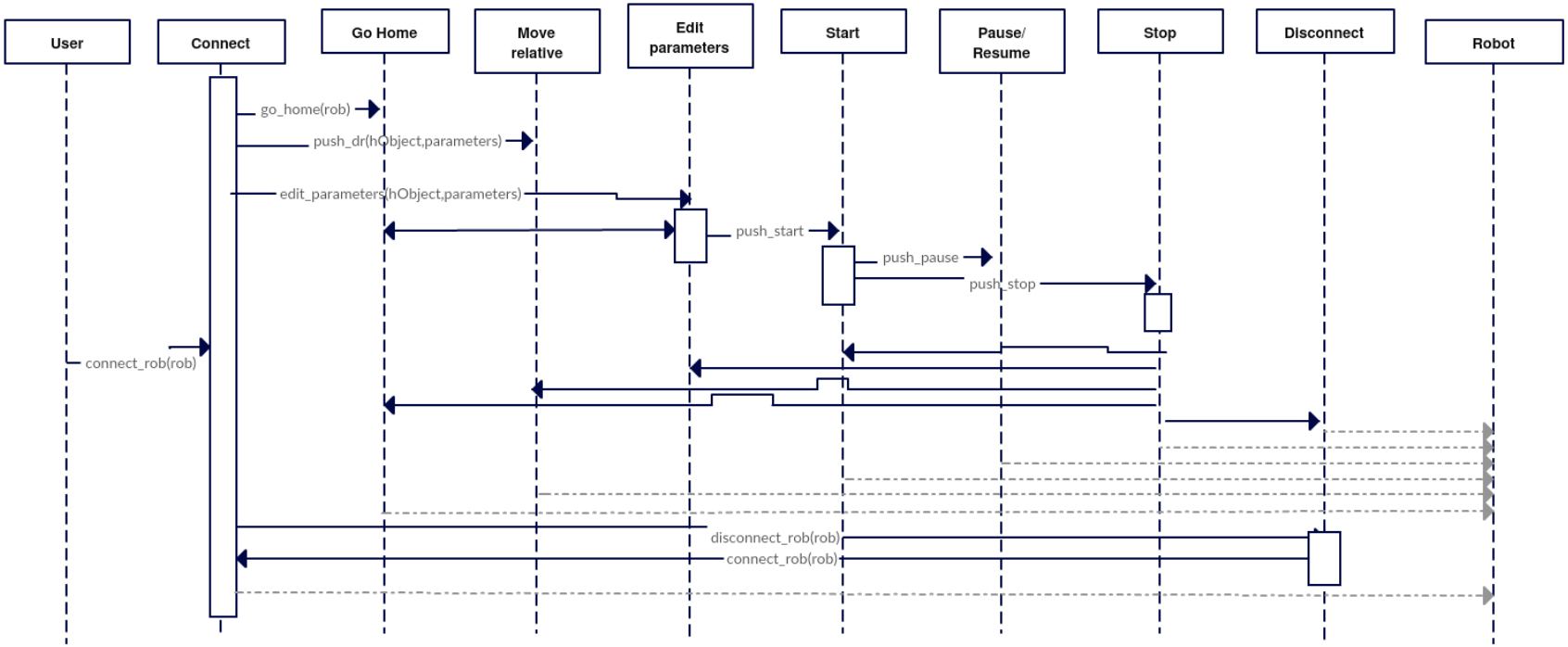
User
Connect
Go Home
Move relative
Edit parameters
Start
Pause/ Resume
Stop
Disconnect
Robot
go_home(rob)
push_dr(hObject,parameters)
edit_parameters(hObject,parameters)
push_start
push_pause
push_stop
connect_rob(rob)
disconnect_rob(rob)
connect_rob(rob)

Appendix D

MATLAB code

Longitudinal Velocity in PVA block samples

```
water_signal=load('water24-3cycles.dat','.mat');        % Loading
 signal from water
sample_signal=load('24sample2-3cycles.dat','.mat');     % Loading
 signal from sample at full transmission

%Redefining mean delay and mean rms values from all samples
t_w=water_signal(:,1);              % Time delay from water
water_s=water_signal(:,2);          % Rms value from water
t_s=sample_signal(:,1);             % Time delay full transmission
sample_s=sample_signal(:,2);        % Rms value at full transmission
T=23;                               % Water temperature [C]
Fs=1./(t_w(2)-t_w(1));              % Sampling frequency [Hz]
N=length(water_s);                  % Signal length [ ]
f=(0:N-1)/N*Fs;                     % Frequency vector [Hz]
d=49.6e-3;                          % Sample thicknes [m]

%Removing the DC value from signals
water_s=water_s-median(water_s);
sample_s=sample_s-median(sample_s);

v_w=1404.3+4.7*T-0.04*T^2;              % Speed of sound in water [m/
s]
Dind=finddelay(water_s,sample_s);
delay=Dind/Fs;
v_l=d/(delay+d/v_w);                    % Londitudinal sample velocity
 [m/s]

% Plotting signals
figure(1);
plot(t_w,water_s); grid on; hold on; axis tight;
plot(t_s,sample_s);
xlabel('Mean delay value [s]'); ylabel('Mean rms value [V]');
legend('Water signal',' Sample signal')
title('Checking delay method');

% Plotting to see the received signal in each case
figure(2);
subplot(2,1,1);plot(t_w,water_s); grid on; box on;
title('Signal without sample');axis tight;
xlabel('Mean delay value [s]'); ylabel('Mean rms value [V]');
subplot(2,1,2);plot(t_w,sample_s); grid on; box on;
title('Signal with PVA sample');axis tight;
xlabel('Mean delay value [s]'); ylabel('Mean rms value [V]');
```

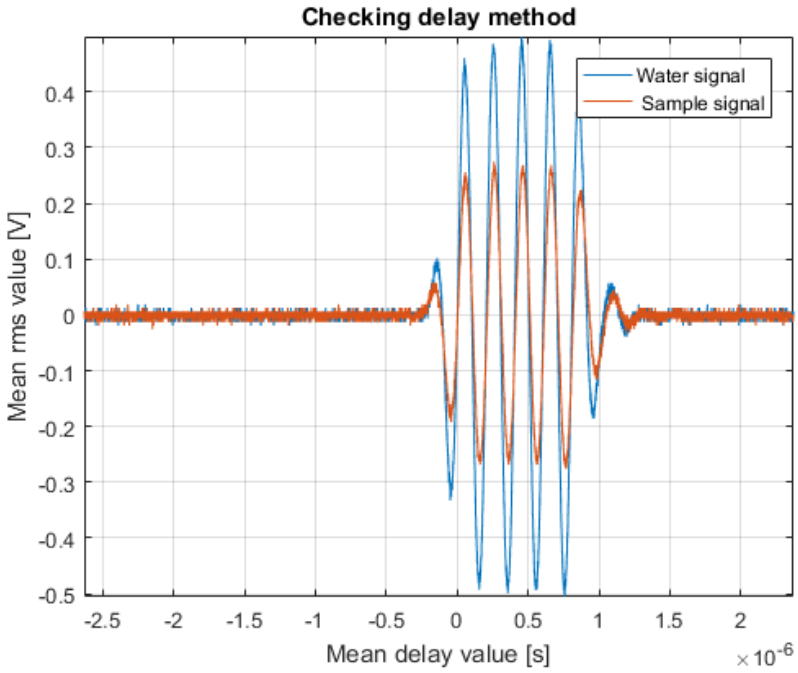
Checking delay method
Water signal
Sample signal
Mean rms value [V]
Mean delay value [s]
×10^-6

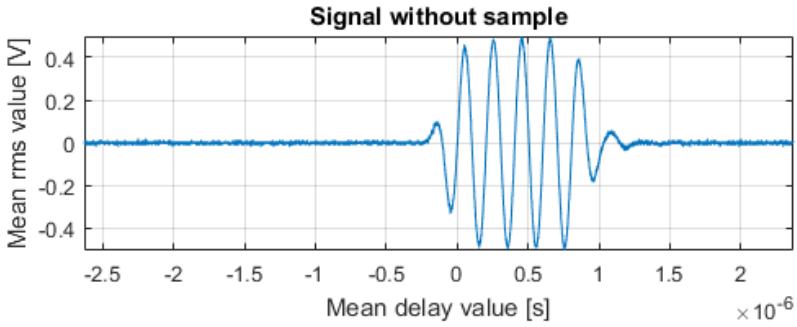
Signal without sample
Mean rms value [V]
Mean delay value [s]
×10^-6

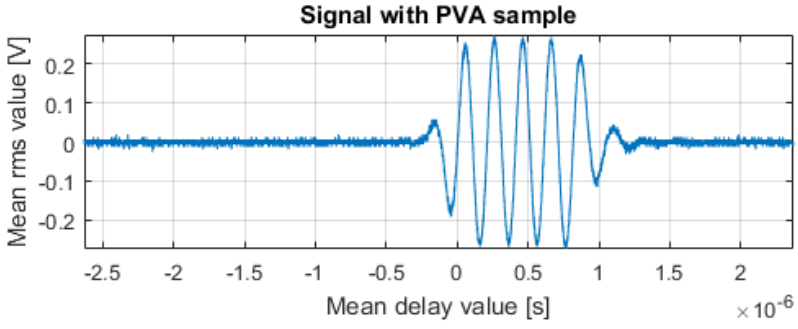
Signal with PVA sample
Mean rms value [V]
Mean delay value [s]
×10^-6

PVA sample characterization

Table of Contents

Longitudinal Velocity

```
data=[  2 1493.13   1495.25     1493.10     1493.00
        3 1494.79    1494.66     1493.50     1493.60
        4 1493.97   1494.81     1491.40     1491.20
        5 1491.56   1491.33     1488.80     1491.20];

cycles=data(:,1);
c0_12_m=mean(data(:,2:3),2);
c0_12_s=std(data(:,2:3),[],2);
c0_24_m=mean(data(:,4:5),2);
c0_24_s=std(data(:,4:5),[],2);

figure;
errorbar(cycles,c0_12_m,c0_12_s); hold on; grid on;
errorbar(cycles,c0_24_m,c0_24_s);
xlabel('Number of F-T cycles [ ]');
ylabel('Sound speed [m/s]');
legend('12 hours cycles','24 hours cycles')
ylim([1488 1496]);
```

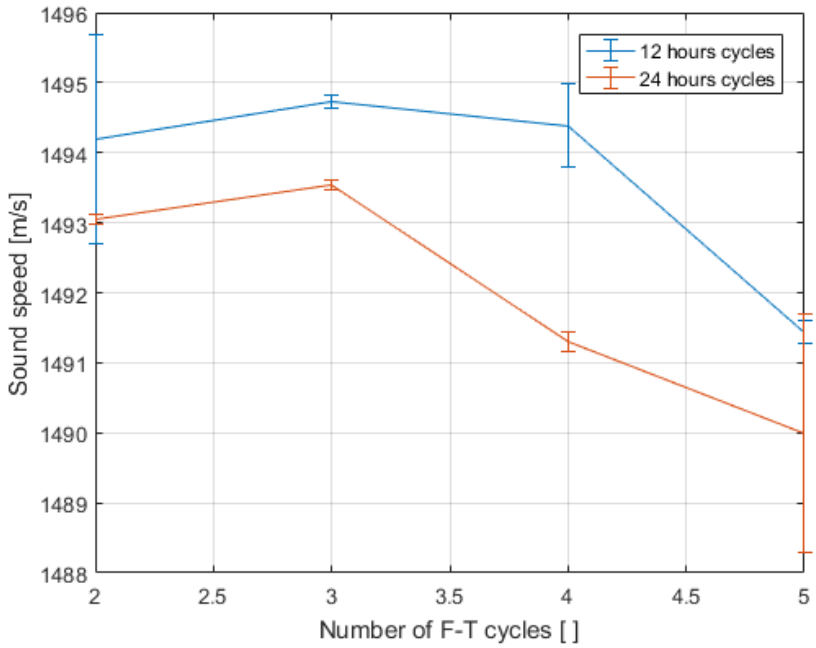

Shear Wave Velocity

```
data=[  2 3.24  0.24 3.11  0.50 3.79  0.49 3.91  0.55
        3 4.27  0.44 4.45  0.35 4.09  0.51 4.24  1.01
        4 5.04  0.56 5.57  0.54 4.71  0.86 4.85  0.58
        5 5.44  1.37 5.85  0.58 5.35  0.63 5.12  0.59];

cycles=data(:,1);
cs_12_m=mean(data(:,[2 4]),2);
cs_24_m=mean(data(:,[6 8]),2);

cs_12_s=sqrt(1/2)*sqrt(sum(data(:,[3
 5]).^2,2)+sum(bsxfun(@plus,data(:,[2 4]),-cs_12_m).^2,2));
cs_24_s=sqrt(1/2)*sqrt(sum(data(:,[7
 9]).^2,2)+sum(bsxfun(@plus,data(:,[6 8]),-cs_12_m).^2,2));

figure;
errorbar(cycles,cs_12_m,cs_12_s); hold on; grid on;
errorbar(cycles,cs_24_m,cs_24_s);
xlabel('Number of F-T cycles[ ]');
ylabel('Shear wave speed [m/s]');
legend('12 hours cycles','24 hours cycles','Position','nortwest')

Warning: Ignoring extra legend entries.
```

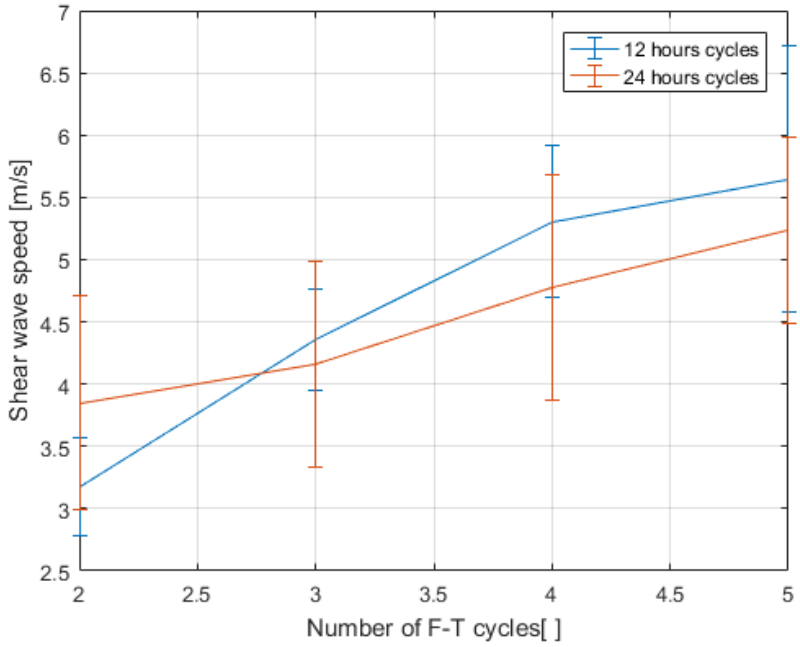

Published with MATLAB® R2016b

SWV with freezing-thawing cycles of 12 hours

Table of Contents

Shear wave velocity for sample 1

```
s1_c2=[3.34 3.37 3.14 3.28 3.07];       % SWV for cycle 2
s1_c3=[4.29 4.22 4.16 4.29 4.38];       % SWV for cycle 3
s1_c4=[4.93 5.21 5.46 4.50 5.10];       % SWV for cycle 4
s1_c5=[5.62 5.13 5.36 5.51 5.60];       % SWV for cycle 5
s1_c6=[6.06 5.67 5.69 5.65 5.67];       % SWV for cycle 5
SWV_1=[mean(s1_c2) mean(s1_c3) mean(s1_c4) mean(s1_c5) mean(s1_c6)]

std_12=[0.16 0.3 0.32 0.20 0.20];       % Standard deviation for cycle
 2
std_13=[0.32 0.25 0.44 0.55 0.63];      % Standard deviation for cycle
 3
std_14=[0.38 0.59 0.76 0.49 0.57];      % Standard deviation for cycle
 4
std_15=[0.48 0.24 0.35 0.53 5.25];      % Standard deviation for cycle
 5
std_16=[0.39 0.86 0.61 0.48 0.59];      % Standard deviation for cycle
 5
std_1=[mean(std_12) mean(std_13) mean(std_14) mean(std_15)
 mean(std_16)]
```

```
SWV_1 =

    3.2400    4.2680    5.0400    5.4440    5.7480


std_1 =

    0.2360    0.4380    0.5580    1.3700    0.5860
```

Shear wave velocity for sample 2

```
s2_c2=[3.17 3.27 2.96 3.06 3.09];       % SWV for cycle 2
s2_c3=[4.37 4.02 4.61 4.70 4.55];       % SWV for cycle 3
s2_c4=[5.32 5.87 5.76 5.52 5.37];       % SWV for cycle 4
```

```
s2_c5=[5.95 5.81 5.70 5.95 5.86];       % SWV for cycle 5
s2_c6=[6.11 5.72 6.50 5.55 5.22];       % SWV for cycle 5
SWV_2=[mean(s2_c2) mean(s2_c3) mean(s2_c4) mean(s2_c5) mean(s2_c6)]

std_22=[0.45 0.82 0.35 0.35 0.54];      % Standard deviation for cycle
 2
std_23=[0.23 0.42 0.38 0.22 0.48];      % Standard deviation for cycle
 3
std_24=[0.35 0.67 0.63 0.65 0.42];      % Standard deviation for cycle
 4
std_25=[0.54 0.49 0.56 0.65 0.65];      % Standard deviation for cycle
 5
std_26=[0.65 0.82 1.16 0.95 1.58];      % Standard deviation for cycle
 5
std_2=[mean(std_22) mean(std_23) mean(std_24) mean(std_25)
 mean(std_26)]
```

```
SWV_2 =

    3.1100    4.4500    5.5680    5.8540    5.8200


std_2 =

    0.5020    0.3460    0.5440    0.5780    1.0320
```

Plotting SWV for both samples

```
cycles=[2:6];
figure(1);
subplot(2,1,1);plot(cycles,SWV_1,'bo-');hold on;
plot(cycles,SWV_1+std_1,'ro');
hold on;plot(cycles,SWV_1-std_1,'ro');
grid on; legend('SWV in sample 1','Standard deviation');axis tight;
ylabel('SWV [m/s]');xlabel('Number of cycles [ ]');
title('Shear Wave Velocity');
subplot(2,1,2);plot(cycles,SWV_2,'bo-');hold on;
plot(cycles,SWV_2+std_2,'ro');
hold on;plot(cycles,SWV_2-std_2,'ro');
grid on; legend('SWV in sample 2','Standard deviation');axis tight;
ylabel('SWV [m/s]');xlabel('Number of cycles [ ]');
title('Shear Wave Velocity');
min_SWV_1=SWV_1-std_1
min_SWV_2=SWV_2-std_2
max_SWV1=SWV_1+std_1
max_SWV2=SWV_2+std_2
```

```
min_SWV_1 =

    3.0040    3.8300    4.4820    4.0740    5.1620
```

```
min_SWV_2 =

    2.6080    4.1040    5.0240    5.2760    4.7880

max_SWV1 =

    3.4760    4.7060    5.5980    6.8140    6.3340

max_SWV2 =

    3.6120    4.7960    6.1120    6.4320    6.8520
```

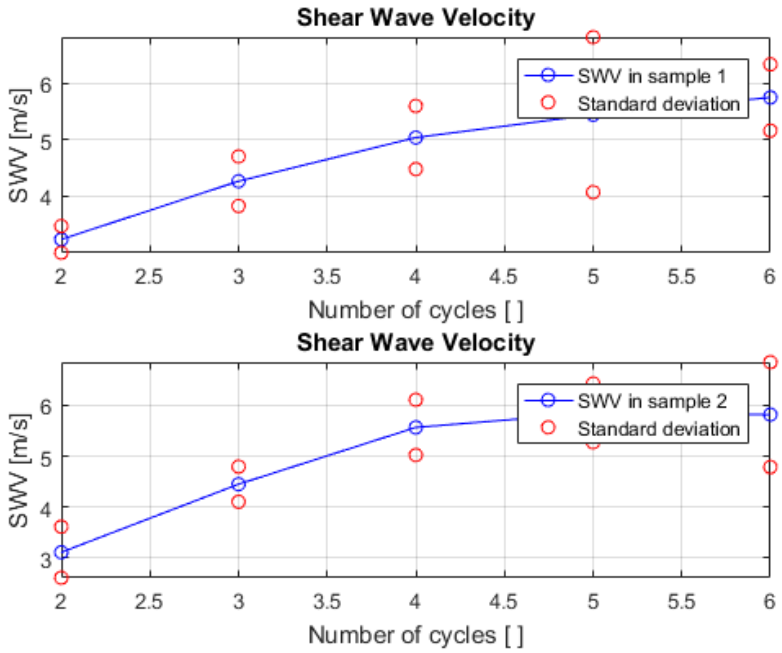

Published with MATLAB® R2016b

SWV with freezing-thawing cycles of 24 hours

Table of Contents

Shear wave velocity for sample 1

```
s1_c2=[3.63 3.79 3.88 3.83 3.82];       % SWV for cycle 2
s1_c3=[3.39 4.11 4.24 4.61 4.10];       % SWV for cycle 3
s1_c4=[4.68 5.19 4.62 5.21 6.52];       % SWV for cycle 4
s1_c5=[5.26 5.29 5.28 5.29 5.65];       % SWV for cycle 5
SWV_1=[mean(s1_c2) mean(s1_c3) mean(s1_c4) mean(s1_c5)]

std_12=[0.37 0.84 0.40 0.43 0.40];      % Standard deviation for cycle
 2
std_13=[0.71 0.43 0.43 0.79 0.20];      % Standard deviation for cycle
 3
std_14=[0.55 1.02 1.07 0.94 1.46];      % Standard deviation for cycle
 4
std_15=[0.53 0.35 1.25 0.26 0.77];      % Standard deviation for cycle
 5
std_1=[mean(std_12) mean(std_13) mean(std_14) mean(std_15)]
```

```
SWV_1 =

    3.7900    4.0900    5.2440    5.3540
```

```
std_1 =

    0.4880    0.5120    1.0080    0.6320
```

Shear wave velocity for sample 2

```
s2_c2=[3.57 3.92 4.05 4.29 3.73];       % SWV for cycle 2
s2_c3=[4.50 4.67 5.23 3.86 5.27];       % SWV for cycle 3
s2_c4=[5.02 4.99 4.48 4.91 4.85];       % SWV for cycle 4
s2_c5=[5.30 5.13 5.06 4.87 5.24];       % SWV for cycle 5
SWV_2=[mean(s2_c2) mean(s2_c3) mean(s2_c4) mean(s2_c5)]

std_22=[0.29 0.61 0.75 0.53 0.57];      % Standard deviation for cycle
 2
```

```
std_23=[0.76 0.78 0.58 0.55 1.64];      % Standard deviation for cycle
 3
std_24=[0.1 0.27 0.87 0.58 1.10];       % Standard deviation for cycle
 4
std_25=[0.87 0.61 0.33 0.58 0.58];      % Standard deviation for cycle
 5
std_2=[mean(std_22) mean(std_23) mean(std_24) mean(std_25)]
```

```
SWV_2 =

    3.9120    4.7060    4.8500    5.1200
```

```
std_2 =

    0.5500    0.8620    0.5840    0.5940
```

Plotting SWV for both samples

```
cycles=[2:5];
figure(1);
subplot(2,1,1);plot(cycles,SWV_1,'bo-');hold on;
plot(cycles,SWV_1+std_1,'ro');hold on;plot(cycles,SWV_1-std_1,'ro');
grid on; legend('SWV in sample 1','Standard deviation');axis tight;
ylabel('SWV [m/s]');xlabel('Number of cycles [ ]');
title('Shear Wave Velocity');
subplot(2,1,2);plot(cycles,SWV_2,'bo-');hold on;
plot(cycles,SWV_2+std_2,'ro');hold on;plot(cycles,SWV_2-std_2,'ro');
grid on; legend('SWV in sample 2','Standard deviation');axis tight;
ylabel('SWV [m/s]');xlabel('Number of cycles [ ]');
title('Shear Wave Velocity');
min_SWV_1=SWV_1-std_1
min_SWV_2=SWV_2-std_2
max_SWV1=SWV_1+std_1
max_SWV2=SWV_2+std_2
```

```
min_SWV_1 =

    3.3020    3.5780    4.2360    4.7220
```

```
min_SWV_2 =

    3.3620    3.8440    4.2660    4.5260
```

```
max_SWV1 =

    4.2780    4.6020    6.2520    5.9860
```

```
max_SWV2 =

    4.4620    5.5680    5.4340    5.7140
```

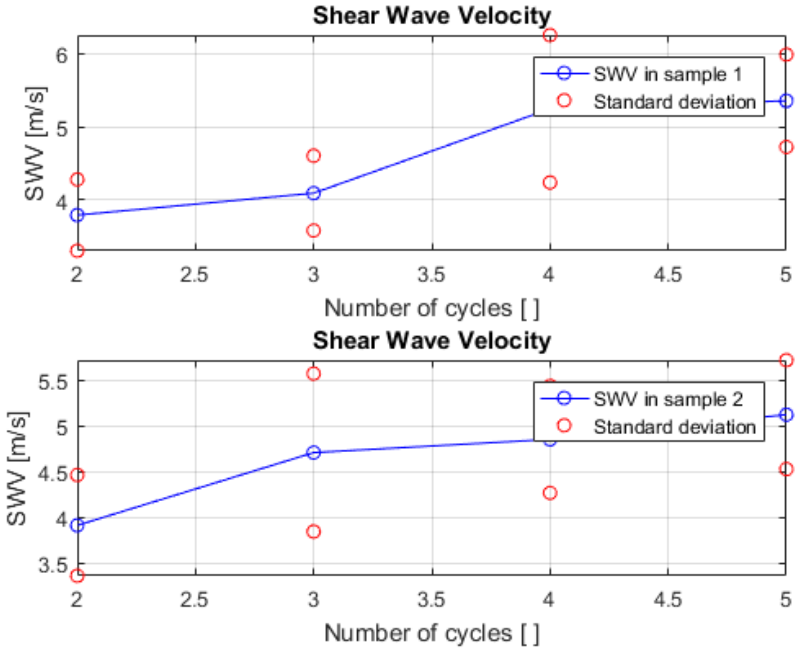

Published with MATLAB® R2016b